Laser-based quantitative studies of minor species in combustion of alternative fuels: Applications of enhanced Raman Spectroscopy

Zubairova, Alsu

2025

Document Version:
Publisher's PDF, also known as Version of record

Laser-based quantitative studies of minor species in combustion of alternative fuels

Applications of enhanced Raman Spectroscopy

ALSU ZUBAIROVA
DEPARTMENT OF PHYSICS | FACULTY OF ENGINEERING | LUND UNIVERSITY

Laser-based quantitative studies of minor species in combustion of alternative fuels

Laser-based quantitative studies of minor species in combustion of alternative fuels

Applications of enhanced Raman Spectroscopy

Alsu Zubairova

DOCTORAL DISSERTATION

Doctoral dissertation for the degree of Doctor of Philosophy (PhD) at the Faculty of Engineering at Lund University to be publicly defended on June 12th, 2025, at 9.15 in Rydberg Hall, Department of Physics, Professorsgatan 1, Lund.

Faculty opponent
Philip L. Varghese, University of Texas at Austin, U.S.A.

Organization: LUND UNIVERSITY

Document name: DOCTORAL DISSERTATION **Date of issue:** 2025-06-12

Author(s): Alsu Zubairova **Sponsoring organization:**

Title and subtitle: Laser-based quantitative studies of minor species in combustion of alternative fuels; Applications of enhanced Raman Spectroscopy.

Abstract: The present thesis was focused on the characterization of carbon-neutral and carbon-free fuels, such as NH_3, DME, H_2 and metal fuels with laser-based techniques. This involved quantitative studies of the flame temperature, major and minor (CH_2O, NO and N_2O) species participating in the combustion process, as well as complimentary studies of CH_2O and H_2/anisole gas-phase mixtures.

The employed laser-based techniques were Spontaneous Raman, Absorption and Polarization Spectroscopy, as well as Laser-Induced Fluorescence (LIF). The work presented the first-ever, to the author's knowledge, quantitative measurements of CH_2O as a flame intermediate, as well as first-ever quantitative measurements of NO and N_2O in a pure NH_3 flame performed with enhanced Raman Spectroscopy, further illustrating the capability of laser diagnostics for flame studies. Additionally, the work also illustrates their potential for interdisciplinary research by applying the Absorption Spectroscopy and the enhanced Raman setup for studies of the time- and temperature-dependent evolution of an $CH_3OH/H_2O/CH_2O$ vapor system, and to ascertain one of the methods for H_2 future studies by checking the anisole tracing efficiency with combined Raman/LIF measurements.

While other studies such as N_2O measurements in a NH_3/Air flame with Polarization Spectroscopy or AlO spectral modeling performed for temperature evaluation of an Al-seeded H_2/O_2 flame did not yield the desired results, they provided a valuable experience, and the acquired unpublished data is also hereby presented.

Key words:

Classification system and/or index terms (if any) Supplementary bibliographical information

Language: English **Number of pages**: 74

ISSN and key title: 1102-8718

ISBN: 978-91-8104-557-4 (print)

978-91-8104-558-1 (electronic)

Recipient's notes Price Security classification

Signature Date 2024-04-28

Laser-based quantitative studies of minor species in combustion of alternative fuels

Applications of enhanced Raman Spectroscopy

Alsu Zubairova

LUND
UNIVERSITY

Faculty of Engineering
Department of Physics

ISBN: 978-91-8104-557-4 (print); 978-91-8104-558-1 (electronic)
ISSN: 1102-8718
ISRN: LUTFD2/TFCP-269-SE
LRCP: LRCP-269

Printed in Sweden by Media-Tryck, Lund University
Lund 2025

Table of Contents

1.1 Abstract

The present thesis was focused on the characterization of carbon-neutral and carbon-free fuels, such as NH_3, DME, H_2 and metal fuels with laser-based techniques. This involved quantitative studies of the flame temperature, major and minor (CH_2O, NO and N_2O) species participating in the combustion process, as well as complimentary studies of CH_2O and H_2/anisole gas-phase mixtures.

The employed laser-based techniques were Spontaneous Raman, Absorption and Polarization Spectroscopy, as well as Laser-Induced Fluorescence (LIF). The work presented the first-ever, to the author's knowledge, quantitative measurements of CH_2O as a flame intermediate, as well as first-ever quantitative measurements of NO and N_2O in a pure NH_3 flame performed with enhanced Raman Spectroscopy, further illustrating the capability of laser diagnostics for flame studies. Additionally, the work also illustrates their potential for interdisciplinary research by applying the Absorption Spectroscopy and the enhanced Raman setup for studies of the time- and temperature-dependent evolution of an $CH_3OH/H_2O/CH_2O$ vapor system, and to ascertain one of the methods for H_2 future studies by checking the anisole tracing efficiency with combined Raman/LIF measurements.

While other studies such as N_2O measurements in a NH_3/Air flame with Polarization Spectroscopy or AlO spectral modeling performed for temperature evaluation of an Al-seeded H_2/O_2 flame did not yield the desired results, they provided a valuable experience, and the acquired unpublished data is also hereby presented.

1.2 Abbreviations

LIF	Laser-induced fluorescence
IR	Infra-red
MFC	Mass-flow controller
HAB	Height above burner
CW	Continuous wave
SNR	Signal-to-noise
AS	Absorption Spectroscopy
PS	Polarization Spectroscopy
DME	Dimethyl ether

1.3 Popular science summary

Combustion has played a significant role in human society for a long time and continues to do so in the present day. It is present in a lot of processes of varying scales, from the heating and electricity plants to transport engines, and to the ones we often do not put a lot of emphasis on since they are so commonplace: candles burning, fireworks, stoves, matches, or campfires.

Just as their scale exists in a wide range, the processes of combustion that are similar in nature tend to vary a lot in terms of the complexity of chemistry and physics involved, the ease of operation as well as the amount of research put into them. For example, while anyone can take some matches and light a candle without any requirements for ambient conditions in mind, the same cannot be said about the ignition of fuel in an engine, even though, at their core, these two flames would rely on the same underlying physical and chemical principles to function.

So, where do the differences come from, and how do they manifest in practice? In applications, several important properties come up, such as the stability of the combustion process, the ease of ignition, types of fuels used (liquid, solid, and gas phase fuels all have their applications), cost of fuels, their storage, and transportation.

Thus, to properly characterize any fuel, one needs to study it starting from the fundamental levels, such as the chemical kinetics of its reactions, with the measurements performed non-intrusively, so that they do not affect the chemistry, in situ at high temperatures (2000-3000 K), often in confined spaces, at elevated pressures (up to 35 times the atmospheric one), and at small (nano- to femtosecond) time scales. One thing that has been discovered to be up to the task and has been receiving more and more recognition recently is lasers, or, more precisely, laser-based techniques.

Lasers also have a variety of applications, from low-power pointers used in class to high-power ones for etching, meaning that there is a large room for adjustments to fit one's needs, which is crucial for flame studies. Since light and matter interact in many ways, directing a laser beam through a medium (a flame, in this case) can generate various kinds of spectroscopic responses – meaning that the light will have different properties before and after passing through the said medium. These property changes can then be converted to important flame data, such as temperature, burning velocity, or species concentrations, all of which are often challenging to obtain with other methods, considering that the flame environment is both hostile and very sensitive to any intrusions. Thus, in recent years, laser-based diagnostics have become rather widespread for combustion studies.

In the present thesis, a variety of laser-based diagnostics is used to either study the flames directly or perform reference measurements that would assist with the characterization of flames or the techniques themselves. The target fuels were chosen with the goal of reducing carbon emissions in mind and are either carbon-

neutral, such as dimethyl ether (DME), or carbon-free, such as ammonia (NH_3), hydrogen (H_2) and aluminium powder (Al).

The most used diagnostic technique in the present thesis is Raman Spectroscopy. While it has definite advantages that make it stand out, such as the possibility for simultaneous measurements of temperature and multiple species, something that most techniques are not capable of, it has a notable drawback of having lower signal intensity than many other techniques, making it challenging to use for detection of minor species (as in, species that are present at <1%). The first set of studies of the DME flames employed a setup for enhanced Raman Spectroscopy, allowing the technique to also detect minor species. This made detecting and quantifying the flame-zone formaldehyde (CH_2O) possible, which was the first, to the author's knowledge, application of Raman spectroscopy for measurements of combustion intermediates in that flame. However, the quantification of CH_2O relied on theoretical data for the Raman scattering cross-section. Thus, additional measurements were performed to obtain its experimental value. These measurements were done with both Raman and Absorption Spectroscopy over a formalin vapor, which then led to a room- and elevated temperature study of the liquid-vapor equilibrium of the $CH_2O/CH_3OH/H_2O$ system that has previously been of interest for chemical modelling.

Then, the multipass setup was applied to study the minor species produced from the combustion of NH_3, a carbon-free fuel that has been gaining attention in recent years both as a stand-alone fuel and also as an H_2 carrier. The primary concerns with using NH_3 are tied to the fact that some of its minor species, such as NO, N_2O, and NO_2, are pollutants, with N_2O, in particular, being a much more potent greenhouse gas than CO_2. Thus, in order to use NH_3 at industrial scales, the knowledge of the exact amount of these species and the conditions for their formation is crucial. In the present thesis, the enhanced Raman Spectroscopy allowed to detect and quantify two of the three species (NO and N_2O) in pure NH_3 flames, which was, to the author's knowledge, the first time the laser-based quantitative data has been reported for these species in a pure NH_3 flame. In addition, N_2O in the NH_3 flames has also been studied with Polarization Spectroscopy, another laser-based technique.

Finally, studies involving H_2 and AlO were performed. For H_2, Laser-induced fluorescence and Raman Spectroscopy were employed to investigate the spatial distributions of H_2 and anisole ($CH_3OC_6H_5$) in laminar and turbulent flows. Anisole is often used as a tracer species for H_2; however, it is a much heavier molecule than H_2, yet there is a lack of studies on how well it follows the H_2 in practice under varying conditions, and the present work is aimed to fill that gap in knowledge. For AlO, a promising metal fuel, a spectral model is developed by the author which then is applied to estimate the flame temperatures in AlO-seeded H_2 flames.

1.4 List of papers and author's contributions

Paper I

Signal-enhanced Raman spectroscopy with a multi-pass cavity for quantitative measurements of formaldehyde, major species and temperature in a one-dimensional laminar DME-air flame. *Combustion and Flame 2022, 244.*

Kim, H.; Zubairova, A.; Aldén, M.; Brackmann, C.

Summary: The multipass setup – a method to enhance the signal of Raman Spectroscopy to a point where it would be possible to employ it to detect minor species in flames – is aligned at 532 nm excitation wavelength and applied to a DME flame to acquire temperature profiles, detect and quantify its major species and CH_2O, an intermediate species that has not been previously measured under such conditions with this technique. The reduction of the required acquisition times provided by the multipass setup proved to be crucial in obtaining the data.

Assisted the first author with setting up the experiment, acquisition of all the data, writing some sections of the manuscript and proofreading it.

Paper II

A study of the liquid-vapor equilibrium of the formaldehyde-water-methanol ternary system – analysis of components and Raman scattering cross-sections. *(Manuscript).*

Zubairova A.; Brackmann, C.

Summary: Following paper I, additional measurements were performed in order to acquire experimental values of spontaneous Raman cross-sections to further characterize the developed methodology. First, measurements with Absorption Spectroscopy were carried out over the vapor-phase formalin system in order to obtain an experimental value for the CH_2O Raman cross-section. Following that, a room- and elevated temperature study of the liquid-vapor equilibrium of the reactive $CH_2O/CH_3OH/H_2O$ system was performed, providing new experimental data to use as a reference for the development of chemical models.

Fully set up both experiments: aligned the optical components, mixed all of the solvents, fixed the issues with the cell and found a way to heat it to desired conditions. Performed all of the data acquisition and data analysis for both cases and wrote the manuscript.

Paper III

Fluorescence-free quantitative measurements of nitric oxide and major species in an ammonia/air flame with Raman spectroscopy. *Proceedings of the Combustion Institute 2023, 39 (1).*

Zubairova, A.; Kim, H.; Alden, M.; Brackmann, C.

Summary: The multipass setup from paper I was applied to measure NO, a pollutant minor species, in an NH_3/Air flame, as well as acquire temperature and major species profiles for the said flame. Similar to the CH_2O measurements, this was the first time NO was detected and quantified experimentally with Raman spectroscopy in the said flame.

Acquired the data together with the second author, analyzed all of the data and wrote the manuscript myself.

Paper IV

Flame structure study of premixed NH_3/O_2/Ar flames using Raman spectroscopy. *Combustion and flame (under review).*
Zubairova, A.; Chen, J.; Konnov, A.A.; Brackmann, C.

Summary: The multipass setup from paper I was re-aligned at 355 nm, where the change in the excitation wavelength allowed significant suppression of flame-zone fluorescence and enabled the acquisition of minor species data in the reaction zone. This was then used to measure N_2O, a minor species and a combustion intermediate, in NH_3/O_2/Ar flames of three different equivalence ratios. Similar to the CH_2O and NO measurements, this was the first time the said minor species was detected and quantified experimentally with Raman spectroscopy in a said flame.

Aligned the multipass system at 355 nm, performed all of the data acquisition for two different flames (the main NH_3/O_2/Ar one under three conditions and the N_2O/CH_4/Ar calibration flame), performed all of the experimental data analysis, wrote the corresponding parts of the manuscript (everything outside of a part of introduction and the chapter on modelling) and proofread the rest.

Paper V

Investigating the Efficacy of Anisole as a Fuel Tracer for Hydrogen.
(Manuscript).
Sridhara A.; Zubairova, A.; Brackmann, C.; Richter, M.

Summary: Anisole is often used as a tracer species for H_2. However, there is a lack of studies on how well it follows the H_2 under varying conditions. In this subproject, the spatial distributions of hydrogen and anisole were investigated in laminar and turbulent flows. Raman spectroscopy was used to monitor non-fluorescent hydrogen, whereas the anisole was traced using laser-induced fluorescence.

Assisted the first author with setting up the experiment, data acquisition, and analysis, wrote some sections of the manuscript and proofread it.

2 Introduction

2.1 Motivation

Recent predictions for the consequences of greenhouse gas emissions further emphasize the need for alternative, carbon-free fuels, particularly for heating and transport sectors that are the main sources of greenhouse gas emissions.

Search for substitute energy sources leads to tests of new types of fuels coupled with looking for ways to increase the efficiency and minimize the harm of already commonly employed ones. Ideally, all the relevant combustion processes should be studied well enough to allow for the development of models that can predict the output (e.g., flame temperature and species concentrations) among a wide range of input conditions (e.g., mixture composition, pressure, temperature, burner or combustion chamber configuration) without the need to carry out experiments for each case. However, since the chemistry of the combustion process is highly complex, with even the most straightforward cases involving hundreds of reactions [1], a substantial amount of experimental data is required for model development and validation. In addition, the flame itself presents an environment that is both extremely hostile to most measurement techniques, and extremely sensitive to any kind of intrusion, further complicating the studies. Thus, there is a need for the development of measurement techniques that can consistently obtain reliable data from a variety of flames.

Over recent years, laser diagnostic methods have been established as one of the most optimal types of methods for flame characterization. They generally fit a lot of the requirements: they are non-intrusive, so they do not affect the chemistry; they can acquire the data in-situ with sufficient temporal and spatial resolution; a lot of the setups and techniques can also find uses in other scientific fields, encouraging cross-field research. However, their development is a constantly ongoing process, and the technique's suitability varies greatly depending on the measurement target. Thus, the main goal of the present work is to ascertain the applicability and limitations of some potential measurement techniques and employ them to provide experimental data that can provide insights into the combustion chemistry that can aid with the development of the kinetic models or assist further research in other ways.

Since intensity of the detected signal scales with the amount of the target species present in the measurement volume, acquisition of data from more abundant (major)

species is more straightforward and can be done with a larger variety of methods. Therefore, the focus of the present studies lands on minor species. They are further relevant since a lot of these species are so-called combustion intermediates, meaning that they exist only in the reaction zone, are directly involved in the main chemical reactions, and, unlike products and reactants, cannot be estimated based on reliable thermodynamic data.

Prior to the beginning of the thesis, a setup that would allow for minor species detection was developed. The setup consists of an aligned multi-pass cavity that is used to enhance the response from Raman spectroscopy signal, which is described in further detail in Section 2.3.3. At the start of the thesis, the said setup was employed for studies of a dimethyl ether (DME)/Air flame and resulted in the successful quantification of formaldehyde (CH_2O) – one of the important combustion intermediate species that is involved in lower-temperature oxidation processes [2, 3]. Then, CH_2O was studied in a different environment as a part of a reactive methanol (CH_3OH)-water (H_2O)-CH_2O vapor system. The abovementioned method was paired with another technique (Absorption Spectroscopy) to cross-check the results. The obtained data was used to aid with the quantification of the prior flame studies.

The following work further employs the same multi-pass setup for studies of ammonia combustion (NH_3). This fuel has been of interest in recent years because it can be used both as a carbon-free fuel and as a hydrogen (H_2) carrier. This would solve the main issues of working with hydrogen – high costs for its storage and transportation as well as corresponding safety risks. However, while it does not involve carbon, NH_3 combustion produces several other harmful species, mostly nitrogen oxides referred to as NO_X. One of them is nitrous oxide (N_2O), which is a greenhouse gas much more potent than CO_2. Thus, before one could consider employing NH_3 on an industrial scale, a very thorough study of the flame composition is required to find a way to minimize pollutant emissions.

In addition to the gas-phase fuels, solid-state fuels such as metals have also been receiving attention as carbon-free alternatives. In this thesis, a molecular model of aluminium monoxide (AlO) is developed to estimate the combustion temperatures of H_2/O_2 flames seeded with aluminium (Al) particles based on provided experimental data.

Already mentioned above, H_2 is also one of the potential alternative fuels. The final part of the thesis presents some preliminary studies performed to ascertain the suitability of anisole as a possible H_2 tracer, which could aid in the H_2 turbulent flame research. This is done by combined measurements employing Raman spectroscopy as well as laser-induced fluorescence (LIF).

2.2 Molecular physics and lasers background

2.2.1 Theory

Research performed in this thesis is primarily carried out with lasers and is based on light-matter interaction, so the present section serves as a brief introduction to the relevant physical processes. The theory is primarily based on the information presented in [1, 4-7]. For more detailed descriptions of laser-based techniques, combustion chemistry or molecular physics background, please refer to these sources.

The section can be started with the introduction of the molecular structure. Each molecule is represented as a combination of atoms, with each atom being a system of a nucleus with electrons orbiting it. Taking a simple molecule like N_2 or H_2 as an example, one can imagine the way it moves in space: since it has two atoms bound to each other, it will have a vibrational type of motion, as if they were a pair of spheres bound by a spring. In addition to translational motion, it will also rotate in space around three different axes, possessing rotational motion. On top of that, each of the atoms will also have the motion of its electronic cloud orbiting the nucleus.

What is of interest to the present thesis is the way this motion ties into molecular energy. If one assumes that each of the types of motion happens independently of the other two (so-called Born-Oppenheimer approximation), the total molecular energy can be represented by a simple sum of the three parts: $E_{mol} = E_E + E_V + E_R$. What has been discovered from theory and confirmed experimentally, is that the values of these energies are discreet and can be represented as levels, with each of the levels having a certain population that reaches towards equilibrium and generally remains constant at constant ambient conditions. A schematic of such a system can be seen below (Figure 1, (a)). The frequency at which each of these motions happens results in all of them existing at very different energy scales, with rotation being around a thousand times slower than vibration and electronic motion being about as much faster. Thus, the schematic only provides a qualitative description of the system, with the distances between vibrational and rotational levels being vastly underestimated.

Now, what happens when one introduces a light source? As it passes through the medium, the light can get absorbed by the molecule, supplying it with additional energy. This energy will then be used to rearrange the population of molecular levels, which will result in the emission of light that can be detected, and the properties of the detected light can serve as a source of important molecular information. Considering how much the energy scales between the three kinds of molecular motions differ, the methodology of choice is then determined by the type of data one wants to acquire.

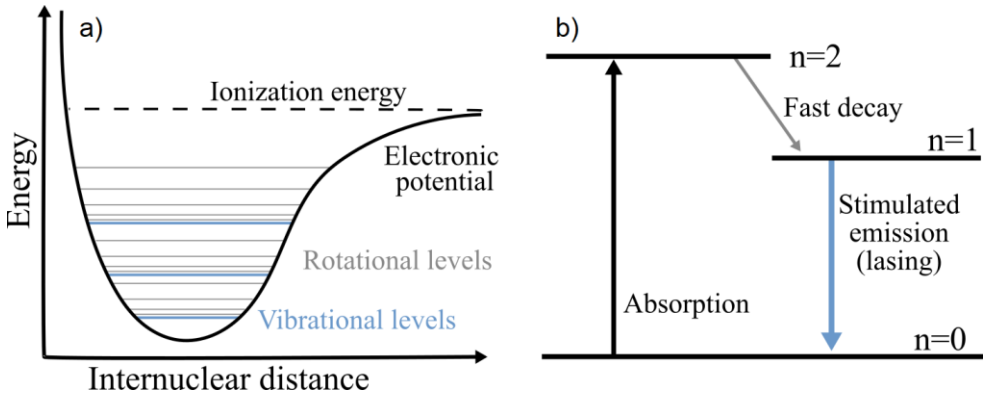

Figure 1. a) An example energy-level diagram of an electronic state with vibrational and rotational levels of a diatomic molecule. b) A diagram describing a three-level system used to acheive lasing.

While there are many various light sources available, lasers in particular stand out due to their flexibility: they can provide both narrow- and broadband excitation of a particular wavelength and also have a variety of other operation parameters (described in Section 2.2.2) that can further adjust the features of the light to suit one's experimental goals, which often leads to lasers being the most optimal excitation choice.

So, how exactly does a laser work? The process can be described as first pumping the medium to create an inverse population (as in, a higher level having a larger population than a lower one), which results in lasing, which then gets trapped in a cavity that selects specific emission lines and further amplifies them. Following the abovementioned energy level theory, a schematic of a system that can be used to obtain lasing can be seen in Fig. 1, (b). Regarding the first step: molecules and atoms can amplify light passing through a medium, but only under the condition of inverse population, given that:

$$\alpha(v) = [N_0 - (g_0/g_1)N_1]\sigma(v) \quad (1)$$

Where $\alpha(v)$ is the absorption coefficient, N_0 and N_1 are the populations of the respective levels, g_0 and g_1 – their statistical weights and $\sigma(v)$ is the absorption cross-section. In the case of $N_1 > N_0$, α becomes negative, meaning that the light passing through the medium gets amplified instead of attenuated. However, the natural population distribution is guided by the Boltzmann law (further discussed in Section 2.3.3), by which inverse population does not occur naturally. Moreover, it cannot be directly obtained between two levels through pumping either, since then the stimulated emission rate will match the stimulated excitation rate, and the overall population of the upper state will stay constant. Therefore, as illustrated in Fig. 1, (b), at the minimum three energy levels are required to obtain inverse population, which then happens as follows: the light gets excited first to an intermediate level

(n=2) which has sufficiently high transition probability to the so-called metastable level (n=1). Metastable levels are levels with longer than average lifetimes, meaning that the molecule would spend longer time on the n=1 level than on the n=2, resulting in the n=1 level having higher population than the n=2 and, consequently, n=0. As a result, the population inversion and lasing are obtained between n=1 and n=0 levels.

Finally, to achieve the desired levels of power and beam monochromacy, the initial laser radiation is trapped inside a cavity. This is again connected to the absorption coefficient: since, normally, light passing through a medium loses its power with distance travelled through it, the reverse becomes true for the amplification in the case of the negative absorption coefficient. However, travelling a long distance through a cavity also introduces certain losses, e.g., from scattering or cavity mirrors absorbing a part of the beam with each reflection to a point where it eventually starts to offset the gain. This then introduces a limit to amplification that can be achieved by a particular system.

2.2.2 Laser characteristics

Some of the relevant parameters for lasers are:

Emission wavelength – as will be further discussed in Section 2.3, the choice of the wavelength one uses for excitation is important: depending on the technique used, it can either strongly affect the signal strength (as for Raman Spectroscopy, for example), or determine whether or not ones get any response from the species of interest at all (Polarization and Absorption Spectroscopy, LIF).

Pulse energy – as illustrated on the left side of Fig. 1, there is a certain level of energy that, if supplied to the molecule, would result in its disassociation. For a good portion of laser-based methods, this is not desired, so there is a limit to how much energy should be supplied per area and unit of time. However, at the same time, the signal of most techniques' scales positively with an increase in laser power, meaning that disassociation can often cause trouble and limit what one can detect.

Repetition rate – for a pulsed laser, referring to the frequency of laser pulses. One of the advantages of having a high repetition rate is the ability to reduce the pulse energy while maintaining the same average power, which allows to enhance the overall signal by effectively increasing the disassociation threshold since one would be able to supply more average power without breaking down the medium.

Pulse length – the length of the laser excitation pulse. As mentioned above, since different types of molecular motion exist on different energy scales and, for photons, energy is directly proportional to the frequency of light, the time scales of the processes one can study depend on the time scale the laser operates at. This means that, for example, a nanosecond excitation can be insufficient for studies of processes happening at picosecond scales and below, such as studies of LIF decay times [8, 9] or non-linear spectroscopy of molecular rotational revival times [10]. In addition, for a fixed pulse, increasing pulse length (also referred to as pulse

stretching) would result in lower peak power, which then can be, similar to increasing the repetition rate, used to avoid dissociation while still preserving the same pulse energy for a stronger signal.

Polarization – laser light, like any light, can be polarized. This means that one of the three vectors used to describe its propagation, the electric one, exhibits a specific type of motion over time. The three types of motion of the polarized light are the circular motion, the linear motion (that can be represented as the combination of the two circular motions in opposite directions) and the elliptic motion (represented as the combination of the linear and circular motion). The laser light is usually linearly polarized and introducing changes to that polarization can be used as a basis for measurement techniques (Section 2.3.2) or to assist with data analysis (Section 2.3.3).

Several types of lasers have been employed in the present work, such as:

- Nd:YAG. A common type of a solid-state laser where lasing is obtained by pumping an Nd:YAG crystal with a flashlamp, with four possible output wavelengths at 1064, 532, 355, and 266 nm, where three of the four have been used for measurements done in the present thesis. The applications also varied: for example, the 532 nm line was used directly for the measurements with Raman Spectroscopy and LIF, while for Polarization and Absorption Spectroscopy it was used for pumping a dye laser. The repetition rates ranged from 5 Hz (LIF measurements) to 10 kHz (Raman Spectroscopy measurements).
- Dye laser. The gain medium consists of an organic dye mixed in a liquid, which relies on an outside light source for pumping, producing a broadband output. Using a cavity to tune this broadband output to a particular wavelength, one can produce any wavelength within the ~350-1100 nm range, which can also be tuned throughout the measurement within a certain range (typically around 20-90 nm), at the cost of having much lower power as compared with, for example, an Nd:YAG. Introduction of an additional mixing unit to perform frequency mixing in non-linear crystals allows to reach the wavelengths within 200 nm – 5 μm range. The present thesis, for example, used two types of dyes – an LDS 867 centred at 860 nm to access the lines for N_2O at 4500 nm and an LDS 821 centred around 815 nm for the CH_2O measurements at 3450 nm, with each of them being tuneable over around 50-100 nm in terms of the final wavelength.
- In comparison, the low-power CW HeNe laser used for alignment of the mid-IR setups of the dye laser system serves as a good example of the flexibility of the laser applications.

2.3 Laser-based techniques

Depending on what is present to be measured in the measurement volume and what type of laser is used for excitation, a variety of different physical interactions can happen. The following chapter elaborates on the physics behind processes that form the basis for the diagnostic methods employed in the current work.

2.3.1 Absorption Spectroscopy

2.3.1.1 Background

Absorption Spectroscopy (AS) is one of the oldest and most well-established optical diagnostic techniques, which works as follows: similar to the way it was illustrated in **Figure 1**, each material has its own energy-level structure with fixed discreet transition lines, which leads to having wavelengths that it mostly absorbs and wavelengths it mostly transmits. As a result, if one shines a laser of a particular wavelength through an absorbing sample with the length l and then compares the signal intensity after passing through the sample I_F with the original intensity I_o, the two will be related based on the Beer-Lambert law:

$$A = \log\frac{I_F}{I_o} = \varepsilon c l \tag{2}$$

Where ε is the absorption coefficient and c is the molar concentration of the absorbing species. In other words, this technique has a straightforward quantification routine that is guided by a single law directly connecting the measured laser intensity to concentration. Another advantage comes from relatively few requirements for the laser source: AS measurements can be performed with both continuous and pulsed lasers, and the required power is very low compared to many other techniques. The last advantage comes from the fact that the final signal is coherent – meaning that it comes in as a part of the laser line that can be collected by the detector with little losses, further increasing the detection limit. What limits the technique application for signal detection is the requirement of suitable tunable excitation wavelength, and what limits the technique application for quantification is the necessary knowledge of the wavelength-dependent absorption coefficient of the target species.

2.3.1.2 Experimental setup

As mentioned above, AS does not require strong laser power. However, it needs a tuneable excitation wavelength, which also covers the range in which the molecule of interest has absorption lines. Since CH_2O and CH_3OH, the target species of the AS studies performed in this thesis, have strong absorption lines in the IR (around

3450 nm), not a lot of systems can readily access them. Thus, the present work ended up employing a more complex setup that is based on the one from [11], as illustrated in Figure 2. Since the output IR beam was invisible, the system was aligned with the assistance of a HeNe laser: shortly after the mixing crystal, the two beams were overlapped, and the visible red HeNe light was then used for the initial setup.

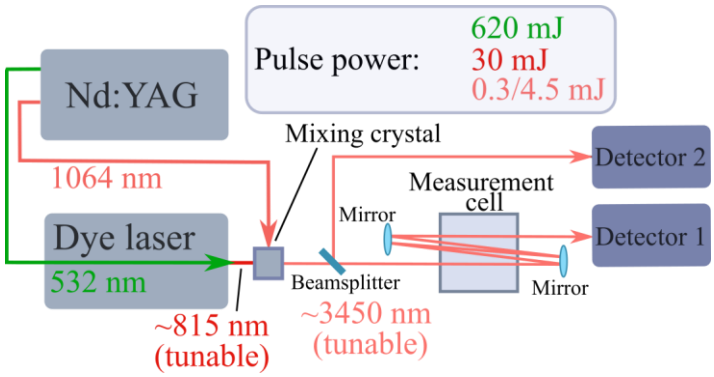

Figure 2. A schematic of the experimental setup employed for the Absorption Spectroscopy measurements. The average power values correspond to the 532 nm Nd:YAG beam (620 mJ), 815 nm dye laser output (30 mJ), and the final output after the mixing unit (0.3/4.5 mJ).

A 10 Hz Nd:YAG laser was used as the primary light source, with the main IR 1064 nm line as well as the green 532 nm frequency doubled second harmonic as an output. The green light was then used to pump the dye laser, and the output of the dye laser was then mixed with the original 1064 nm beam to produce emission in the mid-IR 3450 nm range. As can be seen from Fig. 2, after going through the mixing unit, the final output pulse energy is around 100 times lower than the original 532 nm one. However, this was more than sufficient for the present measurements; in fact, this was already enough to saturate the detectors and needed to be further attenuated. As will be seen with other techniques later, this much power being sufficient is not always the case and can be considered one of the advantages of the technique.

Another advantage is that there is a straightforward way of increasing the detection limit, which is unrelated to the laser power. As can be seen from Eq. (2), absorbance is linearly proportional to the length of the laser path through the target medium. For the present measurements, the target was vapor contained in a measurement cell (**Figure 2**), with optical windows allowing for the laser beam to pass through. Initially, the beam was set to pass a single time through the cell, which was sufficient for measuring high concentrations of absorbing species. However, for the CH_2O measurements, the CH_2O concentration in the cell was too low, so the background fluctuations were strong enough to obscure the relatively weak absorption signal. Thus, **Figure 2** illustrates the final version of the setup, where a pair of additional mirrors were set up in a way that would increase the path length

through the medium. Since absorbance increases linearly with the length of the medium, passing the beam through the volume five additional times allowed to increase it five times compared with the single pass, which ended up being sufficient for CH_2O detection at room temperature and atmospheric pressure. One notable drawback of AS is that the signal increase happens at the cost of spatial resolution, meaning that it will not yield satisfactory results when used in turbulent systems, where one often wants to study the species distribution spatially.

2.3.2 Polarization Spectroscopy

2.3.2.1 Background

Polarization Spectroscopy (PS) is a technique that has similarities with Absorption Spectroscopy: it, too, is a resonant technique that requires a suitable excitation wavelength, which must also be tuned over a certain wavelength range to acquire the resulting spectra; the resulting signal is also coherent, and the required laser power is relatively low. However, in contrast to AS, PS is a non-linear technique, meaning that it scales non-linearly with incident laser power, which is a consequence of it being a result of more complex physical processes compared to AS.

The PS technique relies on probing the response introduced by optical anisotropy induced in a sample when it interacts with a strong, polarized pump laser beam. This is done as follows: the original laser beam is split in two, one weaker (probe) and one stronger (pump), intersecting, as **Figure 3**, (b) illustrates. The pump and probe beam wavelength must match one of the transition wavelengths of the target molecule. The probe beam is linearly polarized, while the pump beam polarization can be either circular or linear at a 45° angle to the probe beam polarization; in this work, circular pump beam polarization is used.

As the pump beam has a different polarization than the probe beam, it interacts with the absorbing medium in such a way that the volume it passes through starts to exhibit properties of a birefringent material, introducing a variation of α (absorption coefficients) and n (refractive indexes) in the medium for the probe beam. This occurs since different polarizations of light drive transitions between different magnetic sublevels in a molecule; a right-hand circularly polarized pump beam, for example, will drive transitions that increase the magnetic sublevel quantum number by +1 (Figure 3, (a)). Since the number of magnetic sublevels is limited by the rotational quantum number of the energy level as (-J, ..., J), a relatively high-level intensity pump beam will generate a nonuniform population of the magnetic sublevels of the molecule. This is equivalent to the angular momentum vector having an anisotropic distribution, which introduces a birefringence in the medium for the linearly polarized probe beam. When the probe beam passes through such a medium, the absorption of the linearly polarized light will slightly change the polarization of the probe beam. The PS technique relies on detecting these small

polarization changes. To this end, the probe beam is aligned through a set of crossed polarizers, which effectively block the probe beam as it passes through a non-birefringent medium (Figure 3, (b)). Then, as the birefringence gets introduced by absorption of the pump beam, the probe beam polarization changes and a small part of it becomes able to pass through the second crossed polarizer and reach the detector. This is what forms the signal beam.

The overall intensity dependence of the PS signal can be presented as follows, as described in [12]:

$$I_{PS} = I_{probe}\left(\xi + \frac{I_{pump}^2 L^2 N_0^2 \sigma^2 \zeta_{JJ'}^2}{16S^2} \cdot \frac{1}{1+x^2}\right) \tag{3}$$

Where ξ corresponds to the residual probe signal not fully blocked by the polarizers, L is the length of the measurement volume, N_0 is the population of the relevant rotational level, σ is the absorption cross-section, S is the saturation parameter as introduced in [13], $\zeta_{JJ'}$ is a parameter related to the polarization of the pump beam, as described in [14] and $x = 2(\omega - \omega_0)/\gamma_s$ is the wavenumber value ω adjusted based on the position of the centre ω_0 and the line width γ_s of the absorption line.

Since the signal scales up with the length of the measurement volume (Eq. 3), which is defined as the area where the two beams overlap (Fig. 3 (b)), maximizing the overlap region of the pump and probe beams by reducing the crossing angle between the beams would maximize the signal.

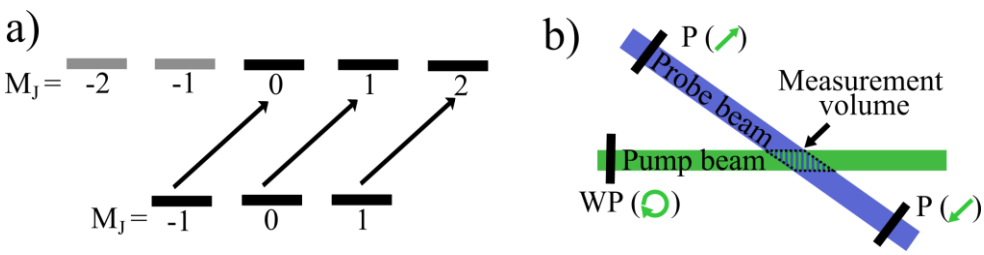

Figure 3. a) A schematic representation of the energy level transitions involved in PS. b) A schematic of the beam arrangement for the PS.

The signal intensity also varies with the degree of molecular transition saturation introduced by the pump beam [15], and working with saturated transitions is advantageous since the PS signal becomes less dependent on the pump laser energy and collisional effects [16, 17]. The empirical signal dependence on saturation can then be introduced as [15]:

$$I_{PS} = A \cdot I_{probe} \cdot N^2 \cdot \left(\frac{I_{pump}/I_{sat}}{1 + I_{pump}/I_{sat}} \right)^2 \quad (4)$$

where *A* is a calibration parameter and *N* is the species number density. Since the PS signal is quadratically dependent on the concentration of the absorbing species, it can be used for quantitative concentration measurements, although in practice calibration is usually required to achieve quantitative concentrations. Calibration measurements are performed by seeding the known amount of the target species directly through the measurement volume; using the obtained footprint signal from a known amount of the particular species allows to estimate their concentration in the target medium. One drawback of a non-linear technique such as PS when employed for species concentration studies at flame temperatures is that the signal decreases quadratically with temperature due to decreasing gas density, unlike some other techniques, where the decrease is less severe. However, the decrease in collisional quenching at flame temperatures compared to room temperature mitigates some of the signal decrease due to decreasing gas density.

2.3.2.2 Experimental setup

The experimental setup (Figure 4) used was based on the same laser system as the Absorption Spectroscopy setup. With an Nd:YAG as the primary light source, the same outputs of 1064 nm and 532 nm were used. However, since the measurements had a different target species (N_2O instead of CH_2O), the dye laser was filled with a different laser dye (LDS867) so that the output after the pumping with the green light was slightly different (centered around 860 nm instead of 815 nm as for the absorption measurements). This, then, after being mixed with the same 1064 nm line, also resulted in the final output with a different wavelength: centered around 4500 nm instead of 3450 nm as for absorption. Similar to the absorption measurements, the target species had absorption lines in mid-IR, meaning that the laser radiation was not visible to the human eye. To that end, a HeNe laser beam, aligned to overlap with the mid-IR laser beam, was used for the initial alignment. The alignment was later optimized by directly looking at the detected signal intensity change and fine-tuning the alignment of the mid-IR pump and probe beams.

The IR laser beam was split into a pump and probe beam by using an uncoated CaF2 class window as a beam splitter, which reflected away ~10% of the laser beam to form the probe beam, while the transmitted light formed the pump beam. The probe beam was aligned through two high-quality Glan-laser YVO_4 (Yttrium Vanadate) polarizers aligned to cross at 90° angle. The first polarizer, transmitting vertically polarized light, was used to ensure the probe beam is entirely linearly polarized as it passes through the measurement volume, while the second one, aligned to transmit horizontally polarized light, was used to block the vertically

polarized probe beam. As the laser beam was naturally linearly polarized as the laser output, the pump beam was sent through a broadband λ/4 waveplate which changed its polarization to circular.

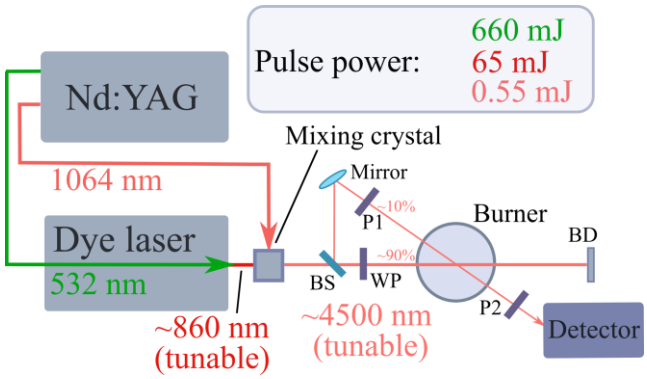

Figure 4. A schematic of the experimental setup that was used for measurements with polarization spectroscopy. BS: beamsplitter, WP: waveplate, BD: beamdump, P1: first probe beam polarizer, P2: second probe beam polarizer. The average power values correspond to the 532 nm Nd:YAG beam (660 mJ), 860 nm dye laser output (65 mJ), and the final output after the mixing unit (0.55 mJ).

Then, instead of the sealed measurement cell filled with gas vapor, a burner with an NH_3/Air flame (either a McKenna one or a Bunsen one, described in more detail in Section 2.4) was placed below the measurement volume, and the PS beam crossing arrangement was set up to cross in the middle of the flame. The same IR detector used for absorption measurements was then used to collect the PS probe beam signal, which was then recorded by an oscilloscope, while the pump beam was blocked in a beam dump. For some of the measurements, a power meter was added to the setup instead of the beam dump to investigate the contributions of the shot-to-shot fluctuations of the laser power to the final noise levels of the signal.

2.3.3 Raman Spectroscopy

2.3.3.1 Background

Raman Spectroscopy is another established technique, and since it is the technique that was employed the most in the present work, the following theory section will be slightly more elaborate. Unlike Absorption and Polarization Spectroscopy, it is incoherent, meaning that the resulting signal is emitted in all directions instead of along a single line. In practice, that means that with incoherent techniques, you cannot collect all the signal, which can lead to higher requirements for the laser power used for excitation. Furthermore, due to its nature, the Raman signal is also much weaker, often requiring additional methods to increase the signal strength. As for its advantages, while it requires strong laser power, it does not require a specific

tuneable wavelength range, can detect multiple species at once, and allows simultaneous extraction of the temperature data. The low signal strength of the Spontaneous Raman process is a consequence of it being a result of inelastic scattering: as the photons interact with the target medium, in most cases, the energy they supply to the molecule is equal to the energy emitted by the molecule because of this interaction. This is called elastic scattering. However, there is a much smaller chance for the energy to get slightly altered in the process, resulting in the incident and scattered light having different photon energies. Since the probability of the underlying process is lower, the average response will also be lower, resulting in a weaker signal as compared with elastic scattering when supplied with equal amount of energy.

Unlike the other techniques discussed in this thesis that require laser excitation to match transitions between existing molecular levels of the target molecule, the Raman process deals with virtual levels that automatically match the excitation wavelength and not the existing ones. In fact, since the Spontaneous Raman signal is very weak and can easily be obscured by signals from other processes (for example, LIF), avoiding strong existing transitions is preferred.

In theory, an excitation source of any wavelength provides a Raman signal. However, since the intensity of that signal scales with excitation wavelength λ as $\sim 1/\lambda^4$, this is not the case in practice. Using an example from the present thesis: a shift from Nd:YAG third harmonic (355 nm) to its second harmonic (532 nm) would result in around four times signal decrease, and going to even longer wavelengths would eventually lead to a point where, while the signal still exists, it becomes too weak to be detected even for major species.

Mathematically, the response of a molecule to incident light can be represented as follows:

$$p = \mu_0 + \sum_{n=1}^{Q} \left(\frac{\partial \mu}{\partial q_n}\right)_0 q_{n0} \cos(\omega_n t) + \alpha_{ij}(0) E_0 \cos(\omega t) + \tag{5}$$

$$+ \frac{1}{2} E_0 \sum_{n=1}^{Q} \left(\frac{\partial \alpha_{ij}}{\partial q_n}\right)_0 q_{n0} \left[\cos(\omega + \omega_n)t + \cos(\omega - \omega_n)t\right]$$

Where p is the dipole moment of the molecule, μ_0 is the permanent dipole moment, the second term is the IR resonant absorption, the third term is the elastic Rayleigh scattering and the last term corresponds to Raman scattering with ω_n corresponding to the molecular motion frequency.

This equation can be used to highlight two important points. First, the $\partial \alpha_{ij}/q_n$ part of the Raman scattering term, where α_{ij} represents polarizability and q_n - normal coordinates of nuclear displacement, defines the main condition for a molecule being Raman active: its polarizability has to change with molecular

motion; otherwise, the term would be zero. This applies to both rotational and vibrational motion separately, meaning that it is possible for a molecule to be Raman active vibrationally, but not rotationally, and vice versa. In addition, for the vibrational Raman, it will be shown later that the dependence on polarizability and dipole moment can be used to filter it out from the background, often being crucial for the data analysis.

The second point is that one can directly see the difference between Rayleigh (with the constant (ωt) term) and Raman (with the $(\omega + \omega_n)t$ and $(\omega - \omega_n)t$ terms) scattering. In fact, these two terms directly represent the two types of Raman scattering: the anti-Stokes one, which describes the cases where the emitted light has higher energy than the absorbed light, and the Stokes type, which describes the opposite. Figure 5 provides a schematic illustration of the three processes in the form of an energy level diagram.

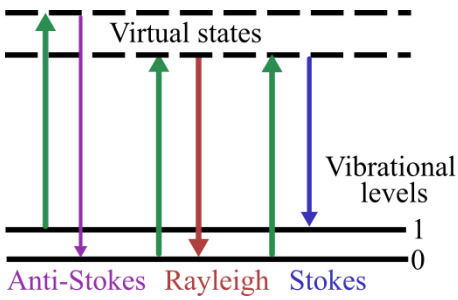

Figure 5. A schematic of the energy level guiding the Spontaneous Raman scattering.

Three features of the Raman Spectroscopy are then further discussed: the temperature evaluation, the quantification routine, and the dependence of the vibrational Raman signal on the polarization of the incident light.

As previously mentioned in Section 2.2.1, the population distribution of molecular energy levels depends on the temperature, and this dependence can be described by the Boltzmann distribution as follows:

$$\frac{N_j}{N} = \frac{g_j \, e^{-E_j/(kT)}}{\sum g_j \, e^{-E_j/(kT)}} \tag{6}$$

Where N_j and E_j represent the population and energy of a particular level, g_j - its degeneracy (as in, if there is more than one level of the same energy), N is the total population, k is the Boltzmann constant, and T is the temperature in Kelvin. Given that this distribution change directly affects the shape of the Raman spectra, with some additional calculations related to transition probabilities, it is possible to model the spectra in a way where the temperature ends up being the primary factor defining the spectral shape. Then, one can vary the temperature so that the simulated

spectrum would match the shape of the experimental one, and the temperature at which they overlap the best would then represent the experimental temperature. Example fits performed on the same set of experimental data using vibrational N_2 models developed by different groups are presented in Figure 6. Both predictions agree within 30 K, which corresponds to <2% uncertainty for flame temperature predictions.

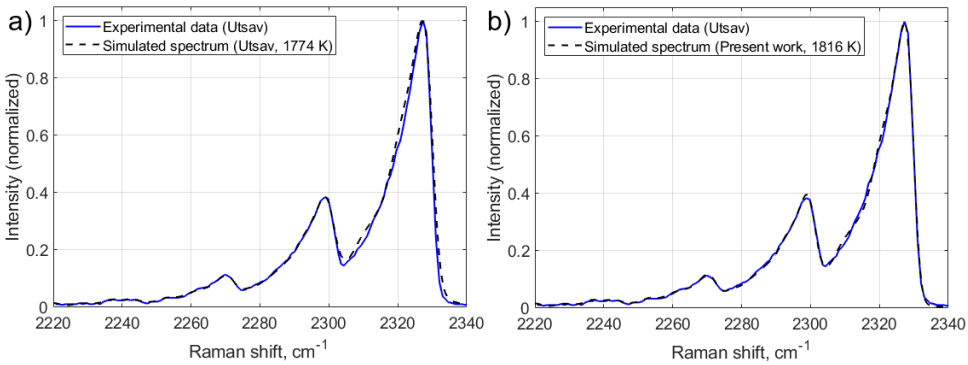

Figure 6. Sample fits of the N_2 spectra for the temperature prediction using vibrational Raman Spectroscopy data. a) Results and model reported by [18]. b) Authors' model reported in [19] applied to the same experimental data.

The species quantification routine of Raman data is as follows: Figure 7 illustrates an example spectrum that has all the species of interest highlighted. If one uses Raman Shift, which positions peaks relative to the laser excitation wavelength, as an x-axis, then each species will have its own fixed position on the spectrum, which could be used to identify it. Then, if one integrates the signal from each species, the integral would be directly proportional to the species mole fraction, with the species' cross-section as the proportionality factor. Thus, if one treats the entire range as a total sum, each species' mole fraction can be evaluated directly. An example of such a calculation performed for the spectrum from Figure 7 would be:

$$m_{total} = \frac{I_{O2}}{\sigma_{O2}} + \frac{I_{N2}}{\sigma_{N2}} + \frac{I_{NH3}}{\sigma_{NH3}} + \frac{I_{H2O}}{\sigma_{H2O}} \tag{7}$$

$$m_i = \frac{I_i}{\sigma_i \, m_{total}} \cdot \chi_o$$

Where σ_i is the species Raman cross-section, I_i is its integral in absolute units and m_i - its mole fraction. The χ_o is used to account for any species present in the measurement volume that are not Raman active. In the case where there are no such

species, this variable should be equal to 1, and if there are, it should be equal to the total mole fraction of these species.

While the calculations themselves are straightforward, various issues can come up in the process. For example, looking at NH_3 and H_2O signals from Fig. 7, one can see that there is a certain overlap, and depending on how it is resolved, the total integral of both species and, thus, their mole fractions would change. Some issues also exist with cross-section evaluation. For example, while the cross-section for each transition stays constant, as the temperature rises, more levels get populated according to Eq. (6), which means that the final cross-section value ends up being an average of the contributions from various transitions. Depending on the molecule, these changes can be either negligible or significant and challenging to estimate (an example of that can be seen in Section 3.2.1 with Raman Spectroscopy measurements of N_2O). Also, since experimentally, the cross-sections are determined by seeding a known amount of the species of interest and then comparing the signal strength to another species of also known cross-section and concentration, acquisition of cross-sections of either reactive species (meaning that their concentration is challenging to establish; such as CH_2O, which is further discussed in Section 3.1) or radicals (meaning that you cannot seed them in general, since they are not stable under ambient conditions) can pose an issue.

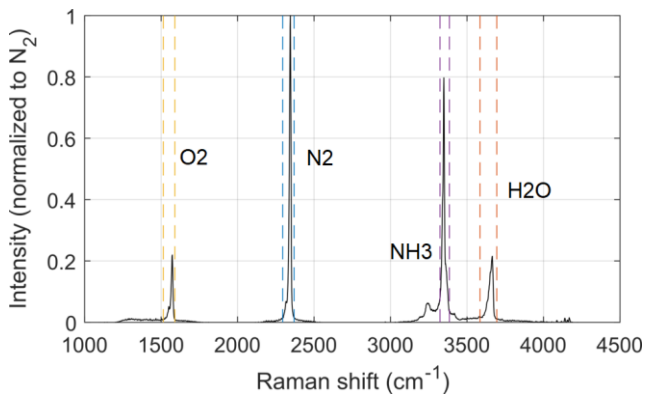

Figure 7. An example Spontaneous Raman spectrum from the reaction zone of an NH_3/Air flame with rough integration channels for the major species highlighted.

The last feature is that, since Raman scattering is connected to polarizability, which is connected to the dipole moment, it is possible to change the polarization of light to significantly suppress the vibrational Raman signal. Change of the polarization is akin to a change in direction from which one perceives the molecular motion and, since the molecular dipole radiation pattern has a donut-like shape, when one looks at it along the direction of the electric field of the light source, a hole it in will be visible. This corresponds to the molecule having no dipole moment along that axis and, therefore, no vibrational Raman activity. In contrast to that,

rotational motion does not have such a directional dependence on the dipole moment, therefore it does not exhibit such a response to the change of the polarization of the light.

In the cases where the desired Raman signal overlaps with some other essentially polarization-independent light signals, such as LIF or rotational Raman lines, this would allow for background subtraction to filter out the desired signal. An example of such a thing can be seen in Figure 8, which shows Raman spectra of NO taken at two different polarizations of the incident laser light. The left part of the signal at around 1820 cm^{-1} overlaps with a rotational Raman line of H_2, which is an issue for the quantification since, as described above, one would require an integral of pure NO, and any outside signal being a part of it would lead to an overestimation of the species mole fraction. Acquiring two spectra at two different polarizations (red and yellow), then subtracting them, allowed to acquire the resulting spectrum (blue), which is a pure vibrational Raman signal.

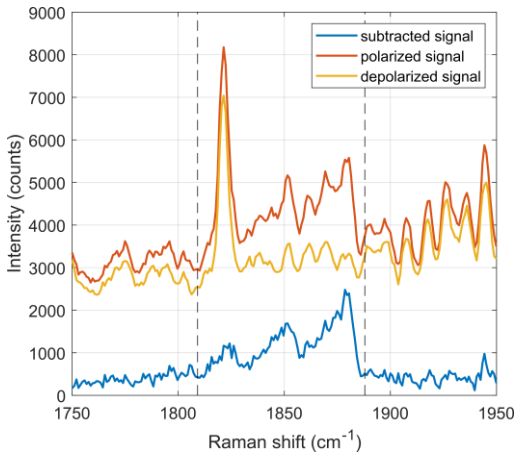

Figure 8. Example spectra of NO from an NH_3/Air post-flame zone taken at different polarizations of the excitation laser. The subtracted signal shows the difference between the signals, which corresponds to the pure vibrational Raman signal of NO.

2.3.3.2 Experimental setup

As mentioned, the Raman signal is on the weaker side, with the final signal also having a strong dependence on temperature due to gas density. Therefore, measuring low-concentration species in flames would require taking additional steps to enhance the signal. Given that the technique is linear in laser power, increasing this parameter should be one of the more straightforward ways. However, the signal from low concentration species is so weak that, for most lasers, one would start ionizing and disassociating the molecules before the signal approaches the desired strength. With that in mind, there are several ways of handling that.

From the laser side, since these processes happen when the molecule receives too much energy in a very short period, there are ways of supplying more energy without reaching the ionization limit; the most common ones are pulse stretching and using a high-repetition rate laser. Pulse stretching means using an optical setup that increases the pulse length (for example, from 10 ns to 150 ns or similar), meaning that, instead of arriving at the same time, the same energy gets slightly dispersed in time, allowing to avoid ionization while keeping the same energy per pulse. Using a high repetition-rate laser approaches this from a different angle: instead of making a long pulse of the same energy, it provides a much higher count of pulses of lower energy, which also allows the energy received by the molecule to be dispersed enough in time to avoid ionization.

From more of the technique or setup arrangement side, another way of increasing the signal intensity is making use of the fact that, unlike some other techniques like LIF, the Raman signal increases with pressure. However, naturally, this is not applicable if one wants to study systems at ambient conditions. Finally, another way of signal enhancement, the multipass arrangement, was employed in the current work for the measurements of DME and NH_3 flames, as well as formalin room temperature measurements.

A schematic of the setup can be seen in Fig. 9. As mentioned before, using a high repetition-rate laser allows to supply high power without inducing optical breakdown; thus, this setup employs a 10 kHz Nd:YAG as the light source, with an average pulse length of around 9 ns and pulse strength of around 3 mJ. To put it into perspective, a 10 Hz Nd:YAG with a similar focal spot size leads to breakdown at around 75 mJ per pulse, corresponding to an average power of 0.75 W. Meanwhile, the present setup supplies the measurement volume with 40 times the average power without inducing optical breakdown.

However, this degree of signal increase is still not sufficient for the detection of minor species at flame temperatures. Thus, an additional signal enhancement technique was arranged as follows (Fig. 9, green line): a cavity was set up by placing two plano-concave round mirrors around 60 cm apart from each other, with one of the mirrors having a hole that would allow the laser beam to enter the cavity. Then, with proper alignment, it would be possible to trap the beam inside for up to 30-40 passes, which would directly result in 30-40 times magnification of the signal. Then, given that Raman Spectroscopy is an incoherent technique, an additional setup of optics would be required to guide the signal into the spectrometer (Fig. 9, red lines). Placing an extra mirror (SM) allows to collect the back-reflected part of the signal to double it in strength.

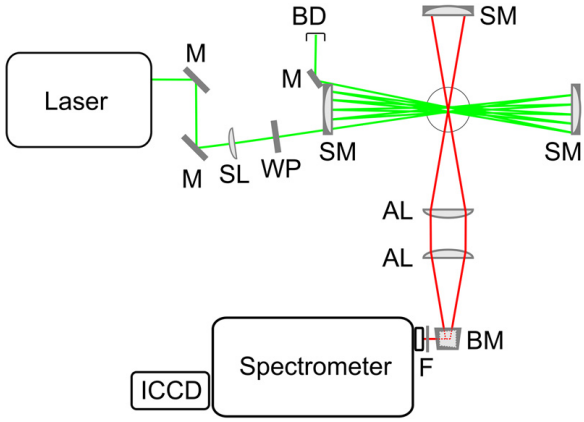

Figure 9. A schematic of a multi-pass combined Raman spectroscopy setup. M: mirror, SL: spherical lens, WP: half-wave plate, SM: spherical mirror, BD: beam dump, AL: achromatic lens, BM: broadband mirrors, F: notch filter, as presented in paper [19].

A more in-depth illustration of the beam arrangement can be found in Figure 10. Various beam pattern arrangements are possible depending on the angle and distance between the mirrors and the focal distance of the lens (Fig. 9, SL) placed before it. In the present work, since the setup was created with the purpose of studying a flat flame, the configuration that had two focal points located at the same height was preferred (Fig. 10, (c)).

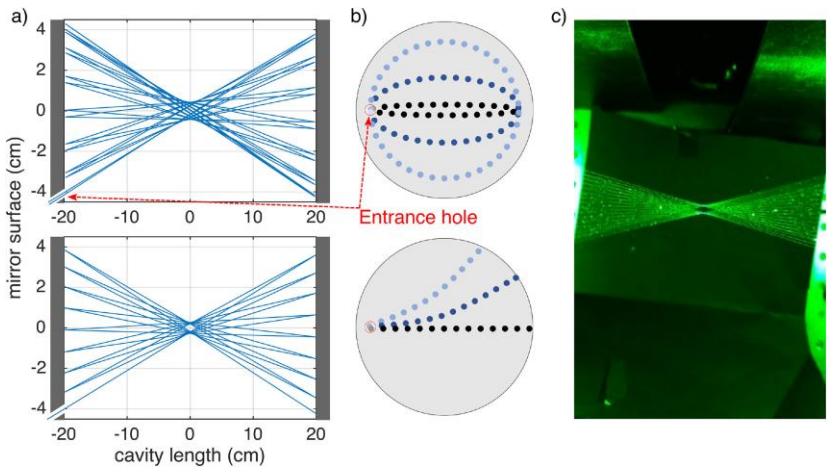

Figure 10. Simulation results of beam paths in the multi-pass configurations. a) Top views of an envelope (ring) mode on the upper panel and two-point mode at the bottom. b) Side views of the reflection spots on the entrance mirror for each mode. c) Photo of the measurement volume from above where the two-point mode is aligned, as presented in paper [19]

2.3.4 Laser-induced fluorescence

2.3.4.1 Background

Laser-induced fluorescence (LIF) is another widespread optical diagnostic technique. It is similar to Absorption and Polarization Spectroscopy in terms of requiring a specific excitation wavelength that would match a particular transition in the target molecule. However, unlike those two techniques, the laser wavelength does not need to be tuneable after the initial setup, which simplifies its practical applications. Even though, like Raman Spectroscopy, it is also incoherent, the fact that it deals with transitions between real molecular levels with much higher probabilities leads to a much stronger signal when excited with the same amount of energy.

In theory, several emission processes can influence the resulting LIF signal. To separate them and provide a level of understanding of their importance, the said processes are outlined in Figure 11. Where in a system of two molecular or atomic levels, the coefficients used to describe the processes are as follows:

- b_{12} – Stimulated absorption. Represents the overall power supplied through the excitation of the target species at the transition wavelength.
- b_{21} – Stimulated emission. A process that is the direct response to the stimulated absorption, with the emitted light aligned the same way as the absorbed light. Depending on the excitation power, it can be both a negligible and a dominant relaxation process.
- W_i – Photoionization. When supplied with sufficient energy, electrons will leave the atomic or molecular orbitals; the existence of ions might affect the overall chemistry of the system and concentrations of the target species. It should therefore be avoided.
- P – Pre-disassociation. Excitation to a state which leads to disassociation, breaking up the target molecule into smaller components will also affect the concentration of the species and is preferably avoided.
- Q_{21} – Quenching. Refers to non-radiative relaxation processes, which usually happen due to collisions between molecules. The fact that LIF is strongly affected by quenching is, for example, the reason it can become weaker at higher pressures, where molecules collide much more often.
- A_{21} – Spontaneous emission is the origin of LIF. The target signal.

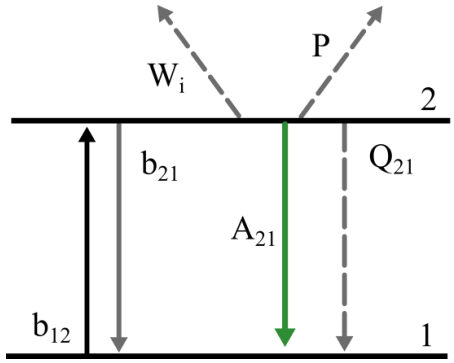

Figure 11. A schematic of the energy-level structure of the LIF-adjacent excitation processes.

2.3.4.2 Experimental setup

A schematic of the experimental setup used to investigate the differential diffusion of hydrogen and its tracer anisole in a turbulent flow field is presented in Figure 12. The simultaneous planar LIF imaging and Raman Spectroscopy measurements were performed over a McKenna burner consisting of a central H_2/anisole jet surrounded by an N_2 co-flow through a porous plug and the flow rates were controlled using MFCs (Bronkhorst, F-201CV-RAD).

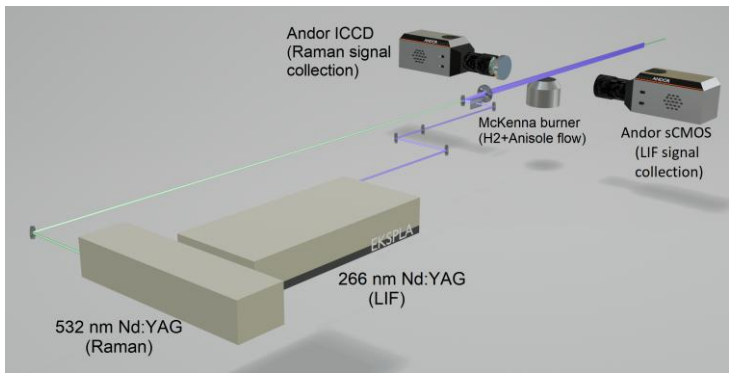

Figure 12. A schematic of the experimental setup employed for the simultaneous Raman/PLIF measurements of anisole in H_2 flows.

An Nd:YAG (532 nm, 8 ns pulse duration) laser was employed for Raman excitation of H_2 and N_2. The laser beam was focused to a 4 mm sheet and the Raman signal was collected at 90° to the laser beam initially using a spectrometer (IsoPlane SCT320) and a PI-MAX4 ICCD camera. While the detection sensitivity of this setup was sufficient for laminar case measurements of N_2 and H_2, where averaging could be performed, it suffered from poor signal to noise (SNR) ratio for the single shot data from turbulent flows. Therefore, to improve the SNR, the collection setup was

replaced with an Andor ICCD camera (Fig. 12) with a bandpass filter (656-686 nm), which resulted in at least 5 times SNR increase.

Planar LIF measurements were conducted using another Nd:YAG laser (266 nm, 250 ps pulse duration) to excite the anisole. The laser beam was expanded to a 30 mm vertical sheet using a cylindrical lens and the LIF signal was collected using a Andor sCMOS camera. A liquid filter (Dimethylformamide) was placed in front of the detector to remove the Rayleigh signal from the laser beam at 266 nm. Five flow conditions have been studied (Table 1, Section 3.2.2), with each condition recorded at three different heights above the burner (HAB).

2.4 Combustion chemistry

Since all of the measurements performed in the present thesis either directly study the flames or are made in order to assist with flame studies, the following section presents a general introduction to the flame parameters and characterization.

So, what is a flame? On the most basic level, to produce a flame, you require an oxidizer and a fuel. While the oxidizer is limited to either O_2 or O_2-containing species, the choice of fuels is much broader. For example, biomass, conventional species like CH_4 or H_2, less conventional species like NH_3, their mixtures of varying fractions or even metals all can act as fuels. Furthermore, while oxidizing species is usually involved as a gas, fuels can also exist in solid and liquid phases, all of which have their own nuance for combustion. Since, outside of the metal fuels, all the fuels studied in the present thesis are in the gas phase, the following section will focus on that while describing the combustion details.

2.4.1 Flame characteristics

Outside of having an oxidizer and a fuel, there are other parameters to be considered. There are two types of flames, depending on where fuel and oxidizer meet. It is possible to make a flame where they are supplied separately and only meet in the reaction zone, which is called a diffusion flame, with common examples being candles and biomass combustion. It is also possible to mix the two before the reaction zone, resulting in a so-called premixed flame. This work is primarily focused on the latter due to flat premixed flames being more suitable for studies of the chemical evolution of the system.

One of the major characteristics of a premixed flame is the equivalence ratio, defined as:

$$\Phi = \frac{\text{Fuel}/\text{Oxidizer}}{\left(\text{Fuel}/\text{Oxidizer}\right)_{stoic}} \quad (8)$$

Where the numerator refers to the mole ratio in the target flame, and the denominator refers to the moles from the balanced chemical equation of the said reaction. Using methane as an example, the reaction equation being $CH_4 + 2O_2 = 2H_2O + CO_2$ means that the fuel/oxidizer ratio is 1:2 and having this exact ratio in the target flame would correspond to $\Phi=1$, the stoichiometric condition. Then, adding extra fuel would produce a $\Phi>1$ flame, which is called rich, and removing fuel would result in an $\Phi<1$ flame, which is called lean. Depending on the goal, either of the three flame conditions can be the preferred one.

Fig. 13 presents examples of the flame structure for two different types of premixed flames based on the photos of the NH_3/Air flames studied in the present thesis. For both cases, the ignited flame burns in the direction opposite to the flow of the fuel/oxidizer mixture, and matching the two allows to stabilize the flame front position. For the Bunsen case (Fig. 13, (a)), the reactants, products and the flame front itself coexist at a given height above the burner, however, for a flat flame (Fig. 13, (b)) these three zones exist at different heights. In practice, this means that if one sends an excitation laser horizontally through the flame, the Bunsen case would provide an averaged signal from all the three zones, while for the flat flame one would only acquire the signal from one of the three zones, and acquisition of the signal from the three zones would require doing several measurements at different heights.

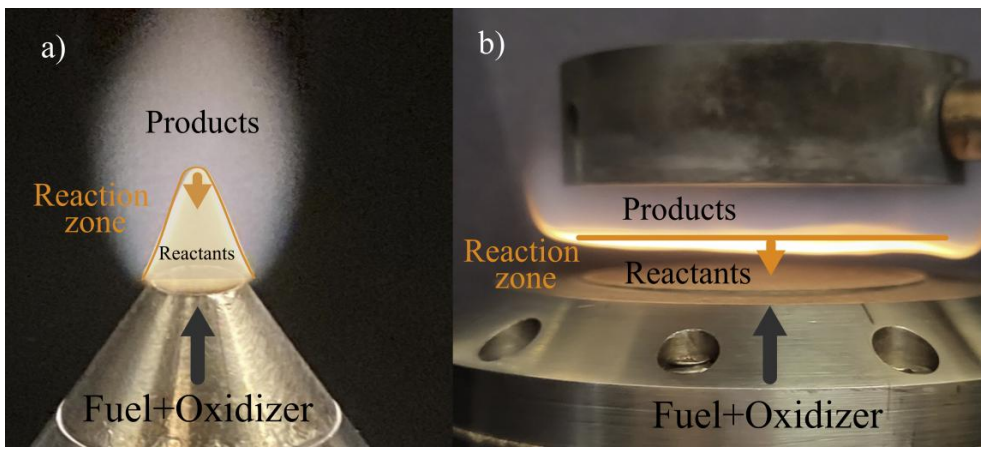

Figure 13. a) Example structure of a premixed Bunsen NH_3/Air flame. b) Example structure of a premixed flat NH_3/Air flame.

2.4.2 Experimental data assistance

Since chemical kinetic models that are used to predict the flame parameters are very complex, with combustion of the fuels with even the simplest molecular composition involving hundreds of reactions, they are mostly validated against the experimental data based on their final predictions of the burning velocity, temperature, and species concentrations, often presented as spatial distributions. However, various techniques may excel or be worse at the experimental acquisition of these parameters, depending on the exact conditions.

While starting and ending concentrations of the products and reactants can be calculated through established thermodynamic data, for intermediate species that only exist as a part of the flame-zone chemistry, the concentrations can only be predicted by chemical kinetics. Raman Spectroscopy and AS probably have the most straightforward quantification routines, unless one must deal with radicals present at low concentrations and/or atomic species, in which case LIF could be better suited.

Vibrational Raman can estimate higher temperatures with better accuracy because that is where vibrational levels get populated. However, rotational Raman works the other way around; thus, depending on the range of interest, either can be the preferred choice. LIF thermometry might be less accurate overall since it often relies on relative values of a few spectroscopic peaks instead of the entire spectral shape, however, LIF also performs better at higher temperatures since more levels get populated and can be used for comparison.

Raman Spectroscopy is the best method for simultaneous multispecies detection. AS and PS, in principle, can detect more than one species with the same light source if both target species have absorption lines in a similar spectral range. However, as mentioned in Section 2.3.2, due to its beam arrangement, the PS signal scales worse with temperature than the other techniques, leading to lower detection limits at the flame temperatures.

Raman also scales the best with increased pressure, while for the other techniques, an increase in pressure results in two opposing processes: the increase in density leads to the signal increase; however, the resulting line broadening and, in the case of LIF and PS, quenching decrease the signal instead.

3 Results

3.1 Carbon-neutral systems

3.1.1 CH_2O measurements in a DME flame

The following section describes DME flame measurements performed with enhanced Spontaneous Raman Spectroscopy setup presented in Section 2.3.3, which are further described in Paper I.

After the initial alignment of the setup, it was time to test it in an actual flame. The aim was to detect combustion intermediate species, in the current case, CH_2O. A 16 l/min stoichiometric flat laminar premixed DME/Air/N_2 flame was set up with a McKenna burner, which was placed on a lab jack to control the height. Then, by adjusting the height, the reaction zone was scanned with a 0.14 mm step. During that, two sets of data were taken: one was a scan of the entire spectral range to evaluate the major species, and another set centred at 2700 cm^{-1} at a higher gain to quantify CH_2O. For both ranges, to account for the background, two sets of data have also been recorded: at vertical and horizontal polarizations, following the vibrational Raman signal dependence on the polarization of the incident light, as described in Section 2.3.3.

The obtained spectra were then quantified using the procedure explained in Section 2.3.3 and plotted against height above the burner (HAB). Two chemical models [20-22] were employed to predict species distribution against HAB. The resulting plots for the major species compared with the kinetic models' predictions can be seen in Figure 15.

Similarly, the CH_2O spectra were quantified against N_2 and compared with the kinetic mechanism predictions (Figure 14). One issue that was discovered was the lack of experimental data on the CH_2O Raman cross-section; as a result, it was estimated theoretically through ab initio calculations based in the data provided in [23, 24] and then compared with experimental data reported under vastly different conditions [25].

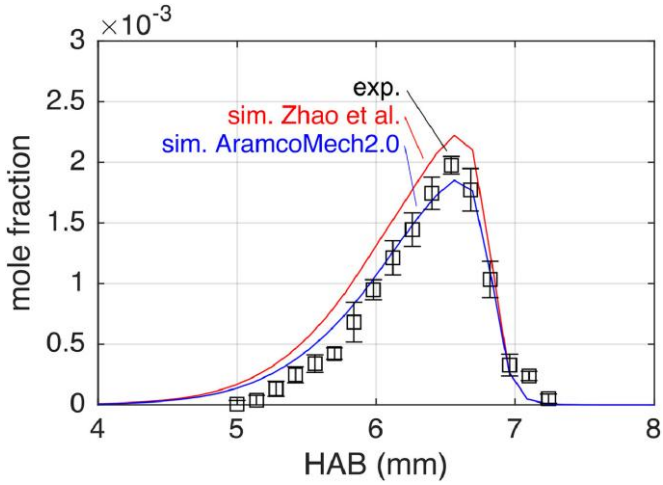

Figure 14. Mole fraction of CH2O in a stoichiometric DME/Air flame at various HAB compared with simulation results of two kinetic models [20-22]. The error bars indicate the standard deviation at each measurement point.

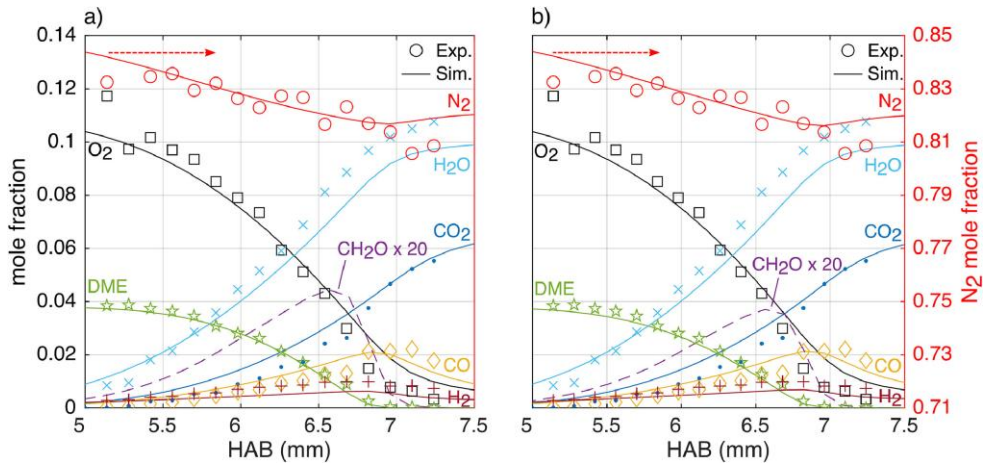

Figure 15. Mole fractions of major species in a stoichiometric DME/Air flame compared with predictions of two kinetic mechanisms [20-22] at various HAB. N_2 mole fractions are plotted on a separate right axis. For formaldehyde, only simulation results are presented, and the mole fractions have been multiplied with a factor of 20 for better display in the graphs, as reported in [19].

In addition, temperature data was derived through the fitting routine described in 2.3.3, with the experimental values showing a good agreement with the model predictions (Figure 16).

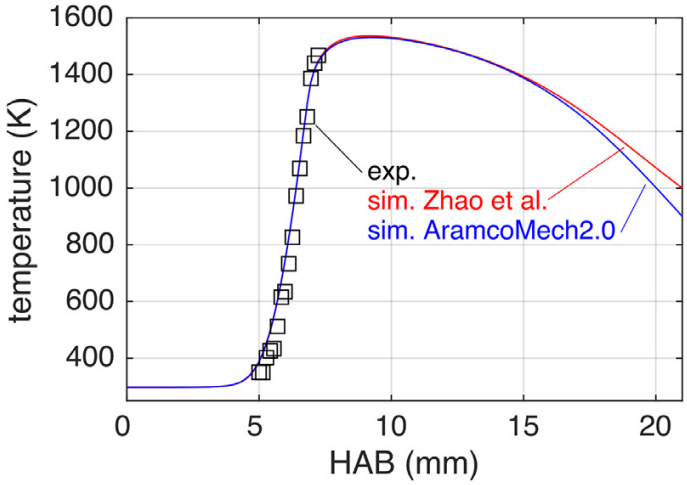

Figure 16. Temperature plot of a stoichiometric DME/Air flame at various HAB compared with predictions of two kinetic mechanisms [20-22], as presented in [19].

In the end, the studies confirmed that the enhanced Raman setup enables sensitive detection paired with shorter measurement times for investigations of stationary or semi-stationary processes. However, while the setup allows for single-shot measurements of major species in laminar flames, its application in turbulent systems can be challenging due to beam steering.

3.1.2 Liquid-vapor equilibrium of formalin-based systems

The quantification of CH_2O from measurements in the DME flames relied on theoretical values of the Raman CH_2O cross-section. Since no experimental values were available in the literature, it was decided to perform additional studies of CH_2O to obtain experimental data on its Raman cross-section. However, this brought attention to original issues with performing such measurements: CH_2O is extremely reactive even under ambient conditions; therefore, the only ways of getting it would be either as a part of formalin (a $CH_2O/CH_3OH/H_2O$ liquid solution), which is commonly used to store it, or by evaporating the paraformaldehyde powder. As the latter required a more complex setup, it was decided to focus on studying formalin.

Since measurements required vapor-phase data, a system with a vapor-phase formalin in chemical equilibrium was established as follows: a 180 ml steel cell with optical windows that allow the laser beam to pass through was employed. A small container of liquid formalin was placed inside, and then the windows were sealed shut. Then, the formalin solvent would gradually evaporate and mix with the surrounding air in the cell, and after around 40 minutes, the vapor-phase system would reach the chemical equilibrium, allowing for estimation of the final concentrations of its components: vapor-phase O_2, N_2, CH_2O, CH_3OH, and H_2O.

While the original goal was the acquisition of the CH_2O cross-section, since the formalin-containing vapor-phase system was reactive, it turned out that the final species concentrations, which are required for the acquisition of the Raman cross-section values, could not be estimated theoretically with conventional equilibrium calculations that are based on the vapor pressure values of the components. Instead, the prediction of the mole fractions would also require a study of the chemical kinetics of the system and the development of an appropriate chemical model. As it was discovered, the said $CH_2O/CH_3OH/H_2O$ system, while having different relative ratios of the components as compared with formalin (28.6/9.4/62% $CH_2O/CH_3OH/H_2O$ liquid phase mole fractions), has already been of interest previously in chemistry and had routines developed that had been tested with experimental data. However, it was also discovered that some of the experimental datasets had gaps that could be filled; in particular, no experimental values for the common formalin solvent employed in the present studies have been previously reported to the authors' knowledge. This then introduced the shift in the original plans.

Instead of using one of the routines to predict the vapor-phase composition and use that data to obtain Raman cross-section directly from Raman measurements, an additional set of measurements was performed, with the entire routine set up as:

- First, Absorption Spectroscopy measurements would be performed to obtain the CH_2O concentration in the vapor-phase formalin inside the cell.
- This data would then be used as a reference for the determination of Raman cross-section values with Raman Spectroscopy measurements performed over the same vapor-phase formalin composition.
- Then, different compositions of the $CH_2O/CH_3OH/H_2O$ system would be studied and quantified directly purely with experimental data obtained in the first two steps.
- This would then allow the acquisition of new datasets for the previously unstudied compositions of the ternary system.
- Lastly, predictions of one of the routines developed by another paper [26], instead of being used as a reference for quantification, would be compared with the new experimental data.

Absorption Spectroscopy results obtained from the first step can be seen in Figure 17. For the initial calibration of the absorption setup, a pure CH_3OH liquid was placed inside the cell, and the $CH_3OH/O_2/N_2$ vapor phase concentrations were studied. Since CH_3OH does not react with air, its vapor-phase concentration can be estimated with phase equilibrium calculations and can be used to compare with the experimental data. In the present work, the calculations predicted 12.8% CH_3OH, while the experimental values fell within 13±0.5%. Then, the same cell was used to measure formalin to obtain the CH_2O fraction at the equilibrium position. This is possible since, unlike the Raman cross-section, the CH_2O absorption profile is well-studied and can be obtained from molecular databases, e.g., HITRAN [27].

Then, the same sets of species (formalin vapor and CH_3OH vapor) were measured with Raman spectroscopy in the same cell, and additional measurements were performed for H_2O in the air to obtain the Raman cross-sections. The final values for the numbers employed to quantify the three species are 1.05 (H_2O), 1.3 (CH_3OH), and 5.2 (CH_2O) $\cdot 10^{-30}\ cm^2/sr$.

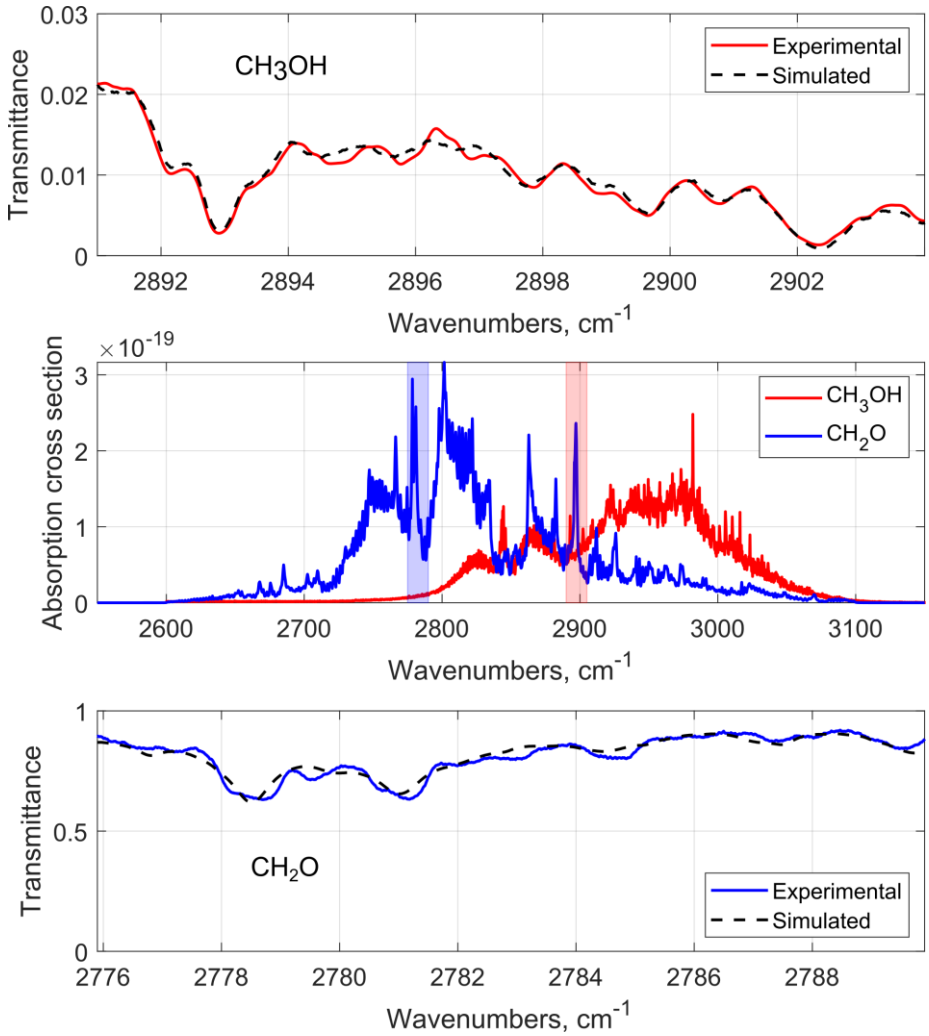

Figure 17. Example fits of absorption spectra recorded from pure CH_3OH vapor (top) and CH_2O vapor from the formalin mixture (bottom) to modelling predictions, as well as the theoretical values for CH_2O and CH_3OH absorption cross-section from HITRAN for the relevant range that were used as the basis for the model (middle).

Following that, a temperature study was performed as the cell was heated from room temperature to around 90 ºC with 10 ºC steps. One of the mixture compositions

(11/21/68% $CH_2O/CH_3OH/H_2O$ liquid phase mole fractions, as reported in [26]) was copied and studied together with the formalin mixture. Figure 18 (a) presents the experimental results of the copied composition compared with predictions of the model developed in that paper. This data shows good agreement, further validating the present methodology and the model performance for those types of mixtures. However, predictions of the formalin mixture (Fig. 18, b) do not show good agreement with the experimental data, with the supposed main reason for that being an increased complexity in chemistry for solvents with higher CH_2O concentrations that the model does not account for. Various methods have been employed to adjust the model to establish a way to still estimate this dependence to decrease this error, but none led to satisfactory results.

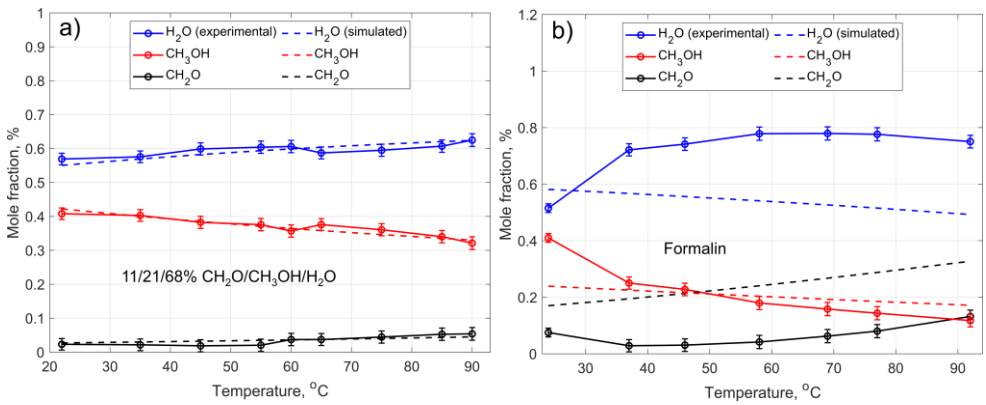

Figure 18. Temperature-dependant composition changes of the two studied systems. Dotted lines represent experimental data from the present study, while solid lines are predictions of a model developed based on the data reported in [26].

Finally, two more sets of room-temperature studies were performed with two fixed CH_3OH fractions (10% and 20%) and varying degrees of CH_2O dilution, and compared with the predictions of that model, with the results presented in Figure 19. The observed dependencies further validate the assumption that the model does not sufficiently cover the more complex reactions at higher CH_2O fractions: while acceptable agreement between present experimental data and the model can be seen for the first two points, the last two points, representing the higher CH_2O fraction, do not match the model predictions at all.

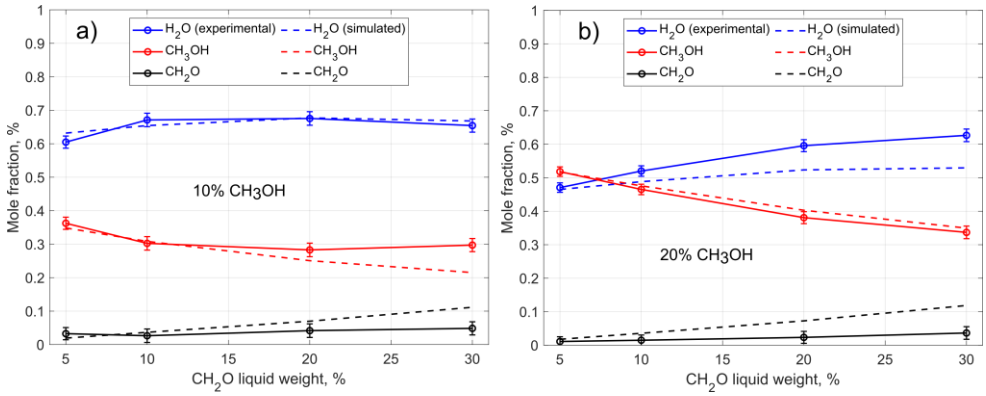

Figure 19. Experimental values for different CH_2O dilution ratios of the formalin mixture, with 10% CH_3OH (a) and 20% CH_3OH (b). Dotted lines represent experimental data from the present study, while solid lines are predictions of a model developed based on the data reported in [26].

3.2 Carbon-free flames

3.2.1 Ammonia

3.2.1.1 NO measurements with Raman Spectroscopy

Following the success of previous measurements of CH_2O in the preheat zone, studies of other minor species have been conducted. For the target flame, NH_3 has been chosen due to its potential as an alternative fuel as well as disagreements in terms of predictions of its pollutant species. There are three species that are worth studying: N_2O, NO_2 and NO. The first two are combustion intermediates, existing only in the reaction zone, while NO is a toxic species that remains in the product zone of the NH_3 flames.

The initial measurements brought an experimental challenge to attention: flame zone measurements in NH_3 flames involving the exact same setup as for CH_2O proved to be difficult due to the extreme LIF background from NH_2 present in the flame zone. While it would be possible to recover major species data, the signal produced by minor species would be fully obscured by the background. Therefore, between NO_2, N_2O, and NO, only NO, which existed outside the reaction zone, ended up being accessible with that setup.

During these measurements, an additional check was performed: while LIF is bound to 532 nm, Raman can work at other excitation wavelengths. With the Nd:YAG having a 355 nm harmonic that, given the wavelength dependence of the Spontaneous Raman, would also provide a stronger signal, it was discovered that the 355 nm excitation substantially reduces the LIF background. While detection of minor species would be initially impossible since it would require setting up the

multipass at 355 nm, replacing all the custom optics, using a single pass at 355 nm would allow for a much more straightforward quantification of major species. Figure 20 illustrates the entire spectral range of a Φ=0.9 premixed laminar NH_3/Air flame scanned with two excitation wavelengths: green for 532 nm and purple for 355 nm, with the latter exhibiting a significant reduction in the background.

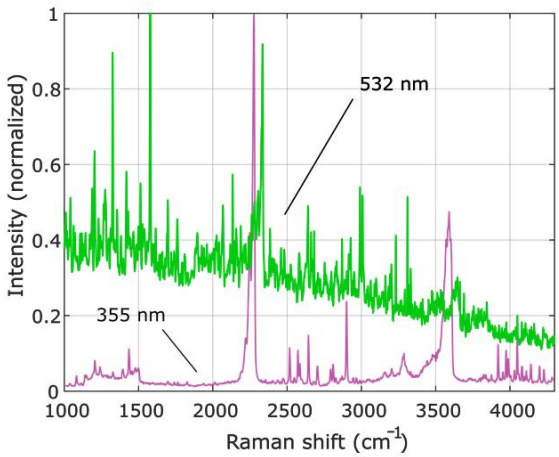

Figure 20. Comparison between two Spontaneous Raman spectra in a lean NH_3/Air flame excited with 532 nm and 355 nm laser lines.

As a result, it was decided to use the 532 nm multipass system for NO detection in the post-flame zone that was free from the LIF background interference, and the single-pass 355 nm system for the major species detection for all HABs. Similar to the CH_2O measurements, temperature profiles for the flames were obtained, and everything was compared with predictions of four kinetic mechanisms [28-31], as presented in Figure 21.

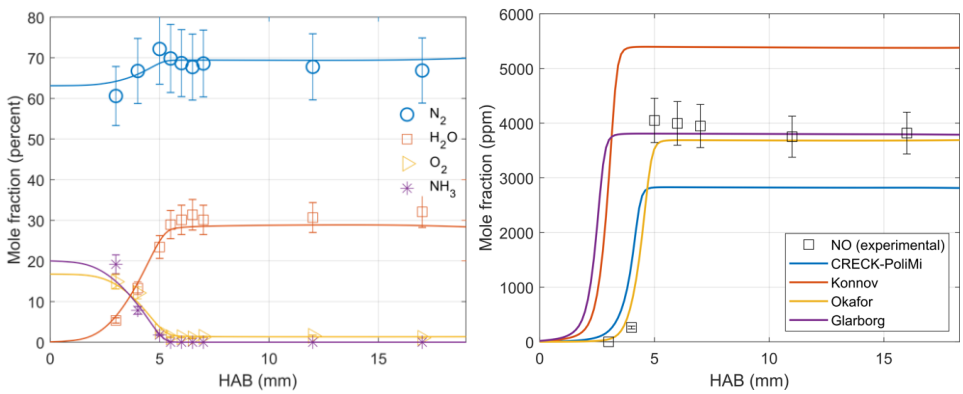

Figure 21. Left: Major species mole fractions from the NH_3/Air flame plotted against HAB and compared

with predictions of a kinetic model [29]. Right: NO mole fractions from the NH3/Air flame plotted against HAB and compared with predictions of four kinetic models [28-31].

Moreover, as discussed in Section 2.3.3, since the Spontaneous Raman cross-section is temperature-dependent, additional high-temperature measurements of the species are generally desired to either study the dependence or at least estimate the error it might introduce. For the most common species, it is straightforward to perform since you can obtain the mole fractions that are required to obtain the cross-section. However, for combustion intermediates or minor species, the acquisition of high-temperature cross-section data can be challenging [32].

In the present work, additional calibration flames have been studied to obtain NO high-temperature cross-section. A lean (Φ=0.7) premixed CH_4/Air flame was established since it normally produces very little (well below 50 ppm) NO [33], and then various amounts of NO were seeded into the flame to study the dependence. An example of the dependence is plotted in Fig. 22.

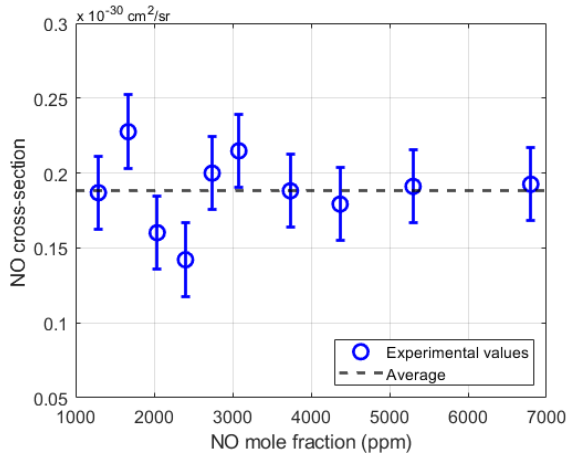

Figure 22. Flame temperature NO cross-section values plotted against the NO dilution numbers from a lean CH_4/Air flame.

3.2.1.2 N_2O measurements with Polarization Spectroscopy

Seeing that the reaction zone Raman measurements of NH_3/Air flames suffered from LIF interference, an alternative technique was tested for N_2O detection in that flame involving a Polarization Spectroscopy setup described in Section 2.3.2. Given that the target species is a minor species, the initial measurements were performed in order to estimate the detection limit at flame temperatures: a 5 L/min N_2 + 5 mL/min N_2O flow was set through a heating tube and heated up to 570 K, with a thermocouple being used to monitor the temperature. The resulting spectra can be seen in Fig. 23, with one spectrum recorded at room temperature (296 K) and the other in a heated gas flow at 570 K. As expected, the PS signal intensity decreases

at higher temperatures, as the signal is proportional to N^2 (Section 2.3.2, Eq. 4), and the number density decreases at higher temperatures. While it was not possible to heat the gas flow up to flame temperatures, the observed temperature-induced intensity changes in these initial tests allowed to estimate that it should be possible to detect N_2O in the flame given the expected N_2O concentrations (as predicted by four different kinetic models in Fig. 23 (a)) in lean NH_3/Air flames.

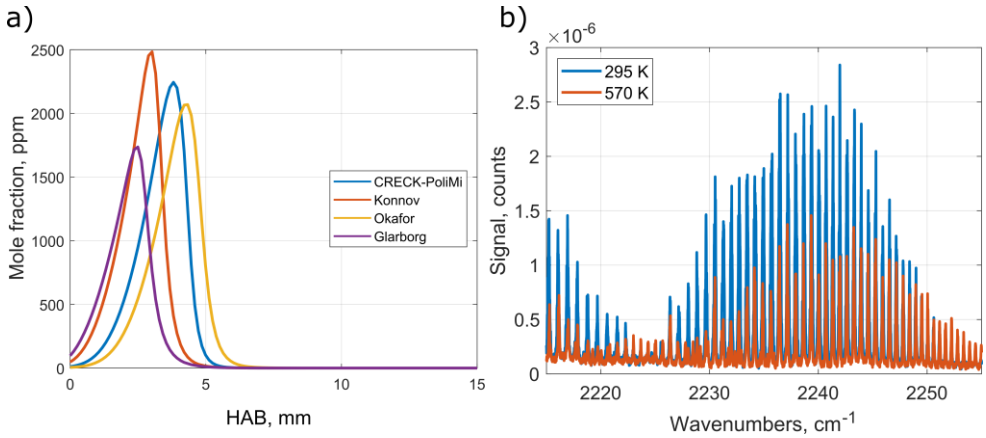

Figure 23. a) N_2O mole fractions against HAB in a Φ = 0.9 NH_3/Air flame as predicted by four kinetic models [28-31]. b) A comparison of the measured signal intensity of an 1000 ppm N_2O flow at two different temperatures.

Since the signal from PS has a quadratic dependence on the length of the interaction region (Section 2.3.2, Eq. 3), the PS experiment was re-aligned to maximize the overlap between the probe and pump beams by decreasing the crossing angle between the pump and probe beams to further improve the detection limit. Absolute signal comparison before and after the realignment can be seen in Fig. 24, which shows the room-temperature PS excitation scans for 250 and 500 ppm N_2O flows with the old alignment and with the new alignment with a smaller crossing angle. As can be seen, the new alignment allowed for the ~5 times increase in detected PS signal. After, the detection limit was estimated in more detail based on the signal-to-noise ratio defined as $SNR = \frac{signal}{noise}$. Assuming the detection limit is reached when SNR=1, the observed intensity changes from Fig. 24 allow for the following calculations: for a constant temperature and pressure, the signal is proportional to the square of the concentration, $I_{PS} = A \cdot c^2$ (simplified from the Eq. 4). Figure 24 (c) allows to obtain I_{PS} as the maximum peak value, and the corresponding noise level. Known values of I_{PS} and c (defined as the seeded N_2O ppm value) allow to acquire the A calibration parameter, the average value for which for the first case before the alignment was 2.01. Then, using the same formula with known A and

setting the I_{PS} equal to the noise value for both 250 and 500 ppm cases leads to an estimation of the average detection limit of 95 ppm.

Performing the same calculations for the spectra acquired after the re-alignment (Fig. 24 (d)) results in an average value of A=12.9 and the corresponding detection limit value of 37 ppm, meaning that the realignment resulted in ~2.6 times decrease of the detection limit at room temperature.

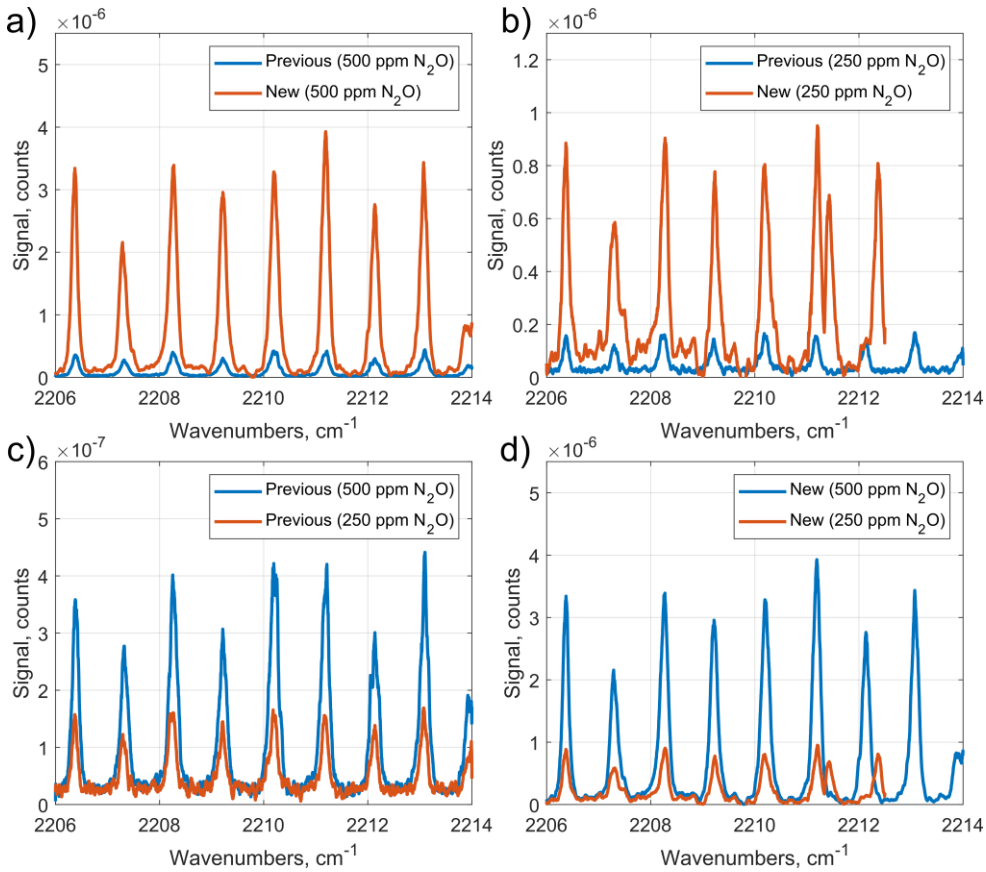

Figure 24. Signal strength comparison before and after the realignment for two N_2O flow conditions (a, b) and relative intensity comparison between these two conditions (c, d).

However, given that the PS signal is not only dependent on the number density, extrapolating the detection limit up from 296/570 K to flame temperatures can be challenging since, for example, levels of collisional quenching and the temperature dependent absorption cross section of the absorption lines also play a role.

These contributions can partially be estimated through simulations. Simulations of signal dependence on number density and simulated absorption cross section show an expected decrease of signal intensity from 296 K to 1700 K by a factor of

2050, however, the simulation also shows 6.7 times decrease going from 296 K to 570 K, while the decrease observed experimentally (Fig. 23) is around 1.8 times, which is significantly lower. This is in line with previous experiments [34, 35], since the collisional quenching that is not accounted for by the simulations, also decreases as the number density decreases with increasing temperature, which leads to an increase in PS signal. As a result, the actual signal decrease with decreasing density is less than what is predicted by the simulations, and often the signal is one magnitude higher at flame temperatures than what the simple simulations would expect. Using the 9.34 experimental quenching correction factor for HCN data from [34, 35] as a reference one could expect around a ~220 times lower signal at the flame temperatures compared to the room temperatures. As the signal is proportional to the concentration squared, a 220 time decrease in signal should increase the detection limit by a factor $\sqrt{220} = 14.8$, so the expected detection limit in flame should be around 600 ppm. However, other factors that have not been accounted for, such as line broadening, could lead to it being up to a factor of two higher in practice.

At last, a Φ = 0.9 NH_3/Air laminar premixed flat flame was set up with a McKenna burner with around 290 ppm of N_2O seeded in it to assist in the initial identification of the spectral footprint of the target species. As the flame temperature was not recorded during these measurements, Figure 25 instead illustrates the absolute detected signal change with height above the burner (HAB). The blue trace was recorded very close (~0.1 mm) above the burner surface, where the temperature was estimated to be close to room one as the burner was water-cooled at a set temperature of 30 ºC. The reaction zone was located ~6.3 mm above the burner, meaning that the measurements taken at 5 mm HAB should present the signal from below the reaction zone, the measurements taken at 6 mm should be close to the reaction zone, while the ones taken at 7 mm should be slightly above it.

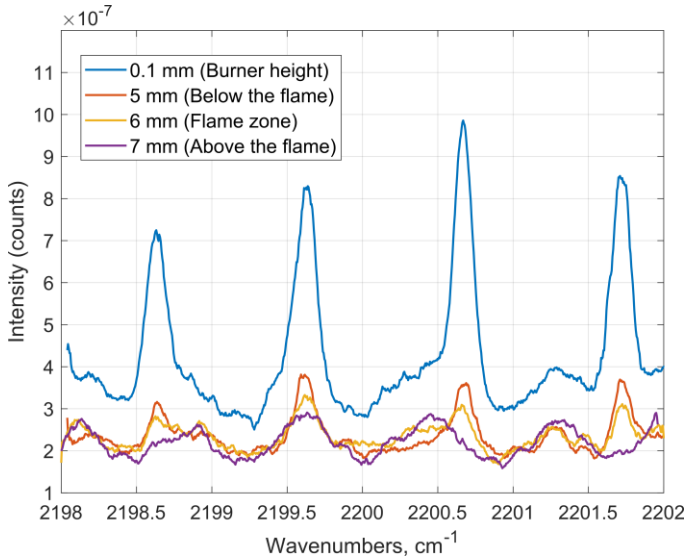

Figure 25. Absolute values of the deteced N_2O signal at varying heights above burner with 290 ppm N_2O seeded in a lean NH_3/Air flame.

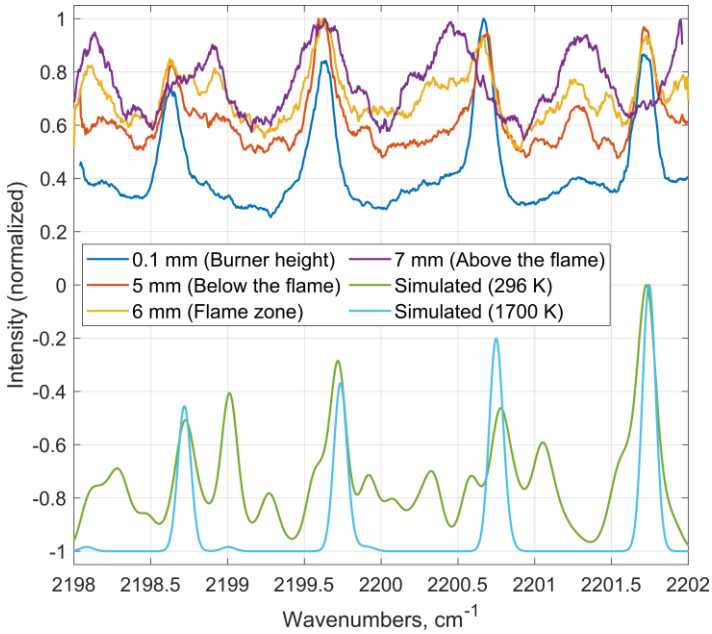

Figure 26. Normalized N_2O spectra from Figure 24 at different positions in the flame compared with the simulation data at room and the expected flame temperatures.

Figure 26 then further illustrates the normalized N_2O spectra presented in Fig. 25 compared with simulation predictions. Despite the signal from the seeded 290 ppm of N_2O being visible in the preheat zone and the flame being expected to have ~2000 ppm of N_2O (Fig. 23, a), none could be detected at the flame height, and there are several factors that could have contributed to that.

One challenge with identifying N_2O lines from the spectra presented in Fig. 26 is that the "background noise" of the signal includes an oscillation, which is most likely caused by periodic variations in the laser intensity due to etalon effects inside the laser. Ideally, PS should be a background-free technique, with the polarizers blocking the probe beam completely; however, in practice, there is a small residual background signal (ξ in Eq. 3) as the extinction ratio of the polarizers is not high enough to completely block the probe beam. As a result, a small amount of laser light can still pass through the second polarizer and introduce an oscillating background to the resulting signal. This can be seen, for example, on the spectrum recorded at 6 mm HAB (Fig. 26, yellow trace) with visible peaks of similar width and intensity. Still, at 6 mm HAB and below, there is clearly a signal originating from N_2O as there are peaks that coincide with the simulation predictions of the N_2O lines, however, at 7 mm HAB the possible N_2O signal gets fully drown out by the noise.

Given these challenges, it also appears that the initial condition for the detection limit defined as 1:1 SNR was not sufficient and in practice it should be perhaps a couple times higher. It should also be mentioned that the detection limit simulated before is merely an estimation, and based on a number of assumptions; for example, the quenching dependence could be different in this case compared to the previous references, which were measured in different species. Lastly, since the laser system did not have an amplifier crystal, which led to a lower output power at these wavelengths compared to the previous quantitative PS concentration measurements [34, 35], it is possible that the saturation condition also was not fulfilled, which means that there was a higher dependence on the collisional effects than originally estimated.

Figure 27 shows a comparison of two scans over the absorption lines performed at around 6.5 mm HAB. In the blue scan, the PS scan was performed normally, while in the red scan, the PS pump beam was blocked. Ideally, since removing the pump beam should remove the N_2O Polarization Spectroscopy signal, comparison between these two scans could be performed to ascertain if the desired signal is still present, even if it is faint. In the present case, the comparison is somewhat challenging to perform as the shot-to-shot intensity variations in the laser beam are different in each scan, but there are no clear differences with consistent peaks between the two scans that could match the N_2O spectral footprint.

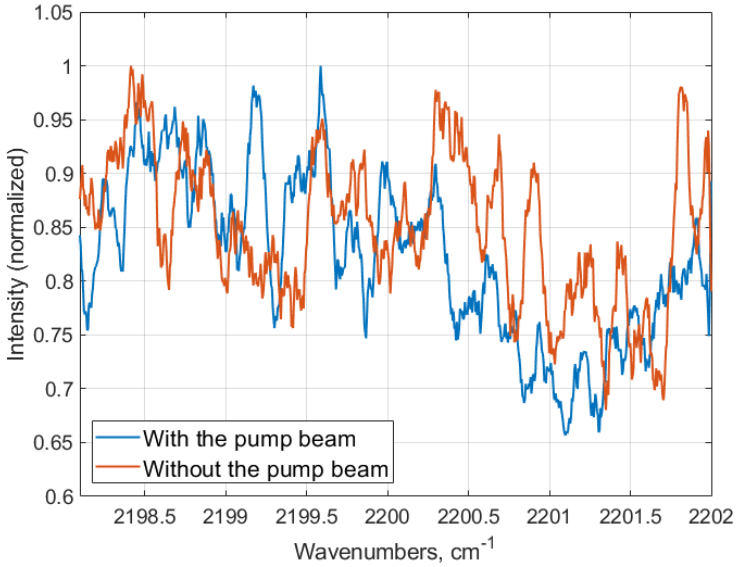

Figure 27. Flame height N_2O spectra taken with and without the pump beam.

Given that N_2O is an intermediate species, one of the reasons for being unable to detect it could have been missing the height at which it peaks. Therefore, for additional tests, a Bunsen flame was set up, which should have the entire profile in the horizontal direction so that one cannot miss the reaction zone. However, these measurements also did not provide any desirable results, and no N_2O could be detected at flame heights. While the challenge with the flat flame was in finding the reaction zone height, the problem with the Bunsen flame was that while we are definitely probing the region where N_2O is present, the said region is very thin compared to the PS crossing volume. As the PS signal is proportional to the square of the length of the crossing volume of pump and probe beams, N_2O only being present within a small fraction of it would lead to a dramatically higher detection limit than previously estimated for the flat flame based on the data from the N_2O flow measurements.

In conclusion, it is very likely that N_2O was present in the flame but the signal was too low to detect it with PS. The estimations of the detection limit for the setup show that it might be on the edge of what could be reasonably detected with PS, and given that the estimation was performed based on a variety of assumptions, as well as the fact that some of the experimental issues, such as low laser power in relation to the saturation condition, have not been accounted for at all, it is completely within the expectations for the resulting signal to be lower than the initial estimation. In addition, the said signal then was further obscured by interference from the background noise, and the unstable NH_3/Air flame made it difficult to target the reaction zone, thus, a decision was made to discontinue the measurements.

3.2.1.3 N_2O measurements with Raman Spectroscopy

Lastly, as mentioned in the 3.2.1.1 Section, a multipass setup was developed for the 355 nm excitation wavelength, allowing for minor species measurements in the reaction zone of NH_3 flames. While it was ultimately possible to detect and quantify N_2O, NO, major species, and temperatures, the experiment ended up involving a fair number of steps.

First, as mentioned before, high-temperature data on the cross-sections was required. However, the acquisition of high-temperature N_2O cross-section data was a bit more difficult than NO. While NO could be seeded in a lean flame, N_2O seeded into a flame generally gets fully consumed in the flame zone anyway, acting like an oxidizer. Thus, instead, a calibration flame with N_2O acting as the primary oxidizer was set up – a laminar premixed $N_2O/CH_4/Ar$ flame. While the original aim was to employ the spectral data from the flame to develop a molecular model that would be able to calculate the cross-section values, like those of O_2 and N_2, this turned out to be not possible with the present setup. The key to these measurements should have been the evaluation of the N_2O temperature-dependant hot band intensities, however, the hot bands could not be spectrally separated with the present spectrometer. Therefore, instead, measurements were performed to identify the error introduced by the temperature-dependent cross-section change to the resulting species mole fractions predictions.

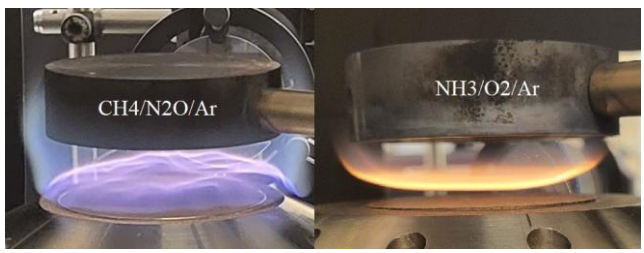

Figure 28. Photos of the two flames studied in the present experiment: the calibration $CH_4/N_2O/Ar$ flame and the main $NH_3/O_2/Ar$ flame.

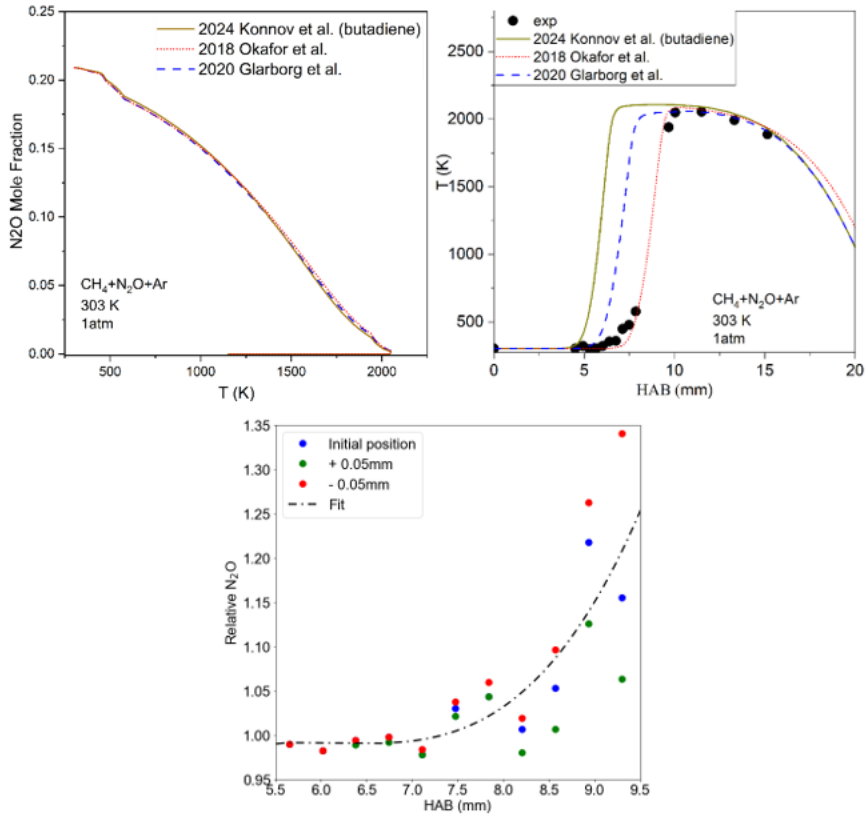

Figure 29. a) Comparison between N_2O mole fraction vs. temperature predictions of the three kinetic models [29, 36, 37]. b) Temperature profiles for CH_4+N_2O+Ar calibration flame. Experimental values (circles) compared with simulations (lines) [29, 36, 37]. c) Ratio between N_2O mole fraction modelling predictions [29] and experimental data evaluated using a room-temperature N_2O cross-section value. The graph represents the temperature dependence of the N_2O cross-section.

The data for these calibration measurements can be seen in Fig. 29. The N_2O mole fraction was estimated in two ways: first was based on predictions of the three kinetic models (Fig. 29, (a)), and second was based on experimental data quantified using the room-temperature Raman cross-section. Then, if one were to match the two predictions against each other based on temperature (Fig. 29, (c)), the observed difference would be equal to the temperature-dependent cross-section change. In the present case, that turned out to be around 15-20% for the relevant temperatures. Some other issues have also been encountered, such as the need for additional resolution of the H_2O/NH_3 or O_2/LIF and N_2O/LIF spectral overlaps, which are described in further detail in Paper IV.

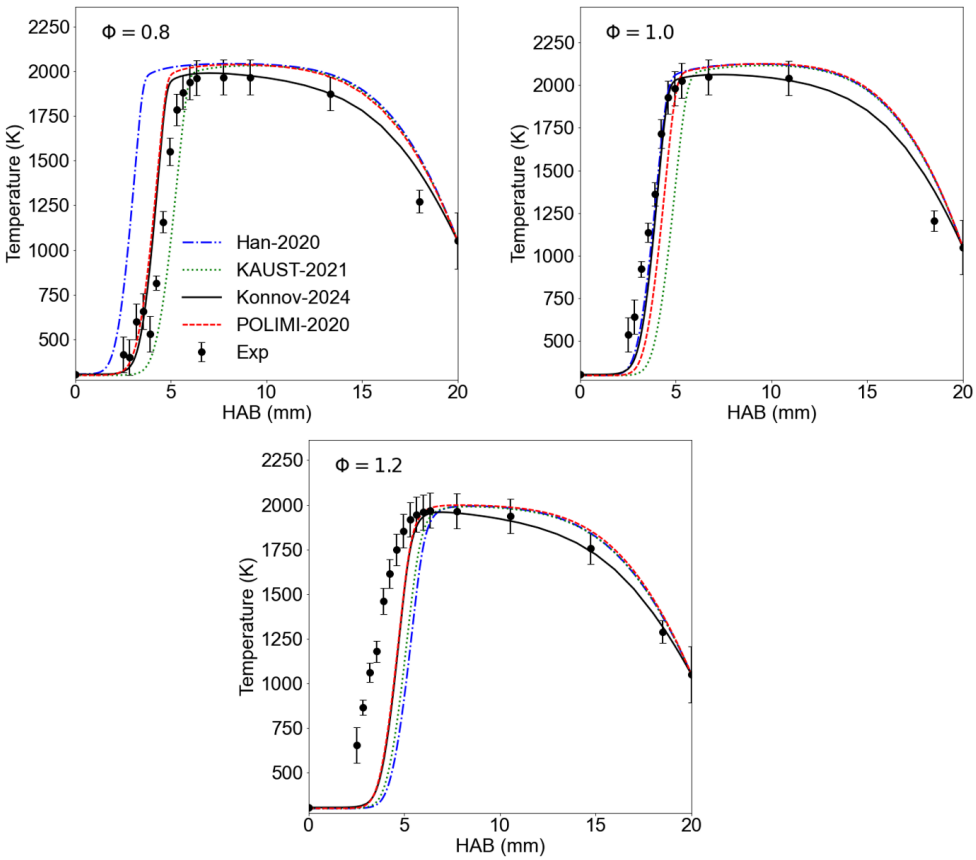

Figure 30. Temperature change with HAB. Experimental values (symbols) compared with predictions of the four kinetic models (lines).

For the main $NH_3/O_2/Ar$ flames, three conditions have been studied: Φ=0.8, 1.0, and 1.2. For each of them, major species, NO and N_2O mole fractions, and temperature profiles have been quantified and plotted against HAB and then compared with predictions of four kinetic models [30, 38-40]. These results are presented in Figures 30-34.

In Figure 30, presenting temperature data, some disagreements with the kinetic model predictions can be observed for the lower temperature data. This can be explained by the fact that temperature predictions were performed by matching N_2 spectra to the simulation predictions, however, since higher vibrational levels only start getting populated at temperatures above 500 K, very little change in shape is observed at lower temperatures.

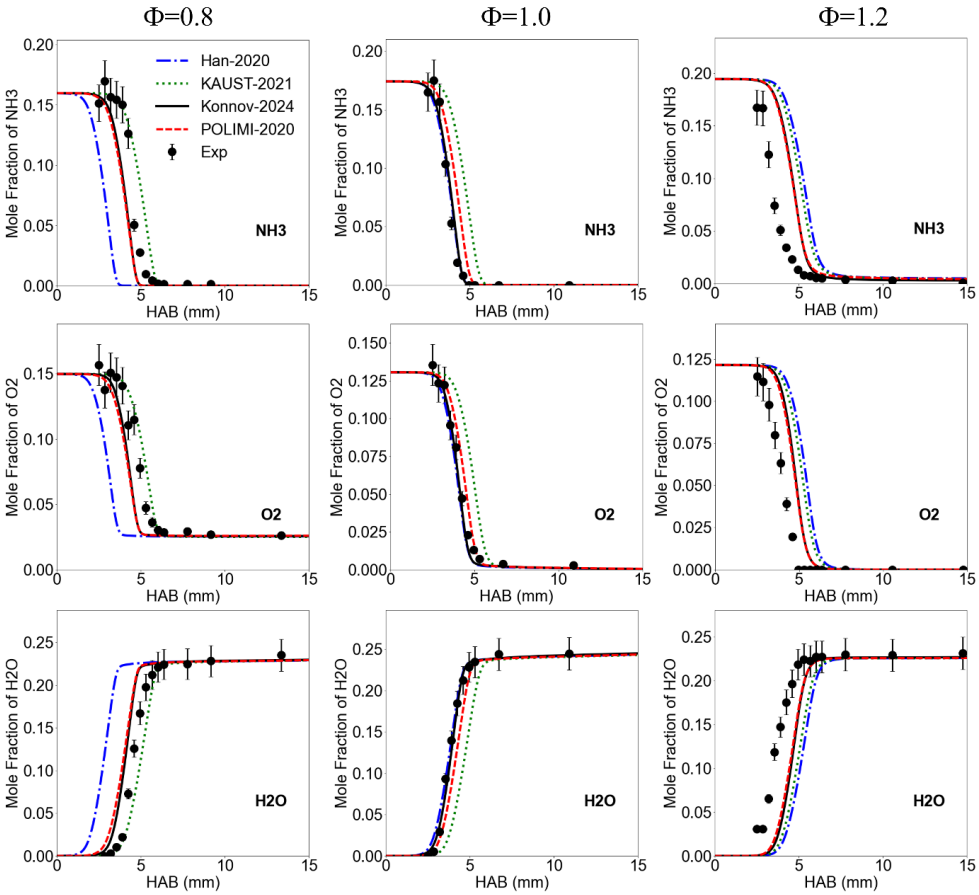

Figure 30. NH_3, O_2, and H_2O mole fractions change with HAB. Experimental values (symbols) compared with predictions of the four kinetic models (lines).

Figures 31 and 32 present the major species mole fraction data. While overall agreement is observed, especially when it comes to final mole fraction predictions, some of the preheat zone points (e.g., the second point of O_2 and NH_3 for the lean case) show notable deviations. One of the possible reasons for that could be insufficient averaging: in the preheat zone, in particular, strong oscillations of the multipass arrangement have been observed.

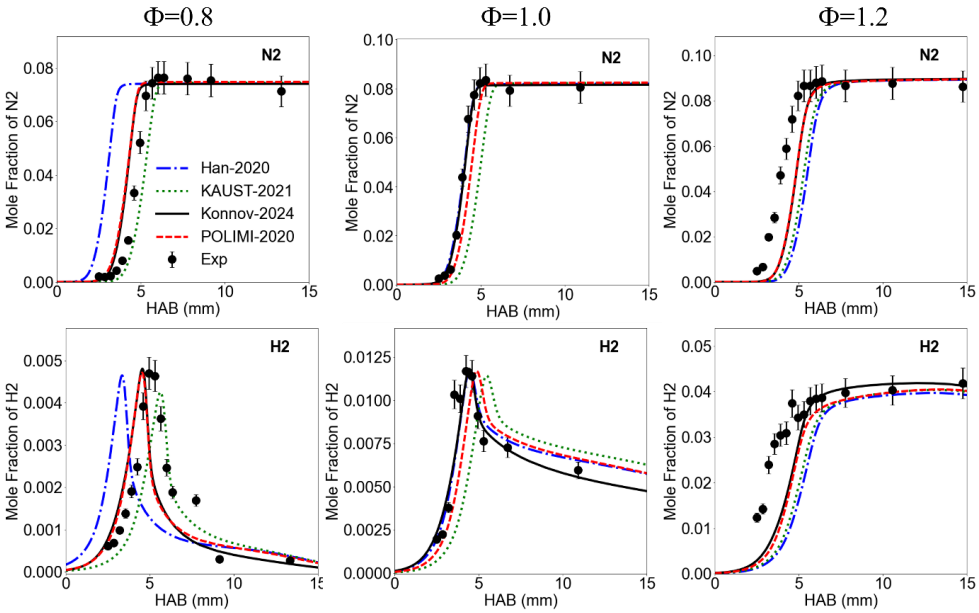

Figure 31. N_2 and H_2 mole fractions change with HAB. Experimental values (symbols) compared with predictions of the four kinetic models (lines).

Figures 33 and 34 present the NO and N_2O mole fraction evaluation results. The respective detection limits for NO and N_2O have been estimated to be 500 and 600 ppm, respectively. Following that, mole fraction values that fall below these limits have been presented as a part of the profile without the error bars.

For NO, the experimental data follows the expected behaviour, with higher values being observed at lower equivalence ratios and the species being fully consumed around the reaction zone for the rich case. Overall, NO mole fraction predictions also exhibit acceptable agreement with all of the kinetic models, considering the error bars.

For N_2O, while the experimental data also follows the expected equivalence ratio dependence, not all the models have been able to predict it with sufficient accuracy.

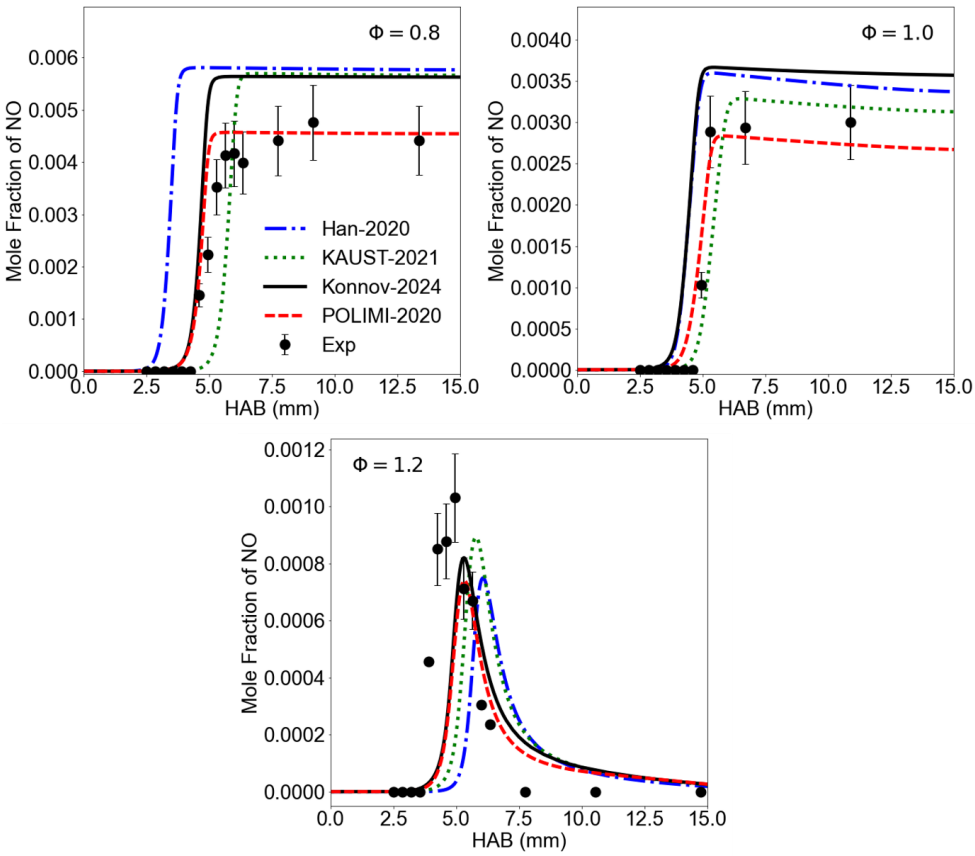

Figure 33. NO mole fraction change with HAB. Experimental values (circles) compared with predictions of the four kinetic models (lines).

In the end, the ~30 times signal enhancement provided by the multipass allowed to reduce the accumulation times by the same amount, with the measurements at each HAB taking around 5 minutes instead of 2.5 hours as a result, which made performing them realistically feasible.

However, calibration measurements ascertained that a higher resolution spectrometer would be necessary for improved N_2O characterization, and for further NH_3 flame studies with the 355 nm excitation one would have to identify the source of fluorescence to learn its exact footprint.

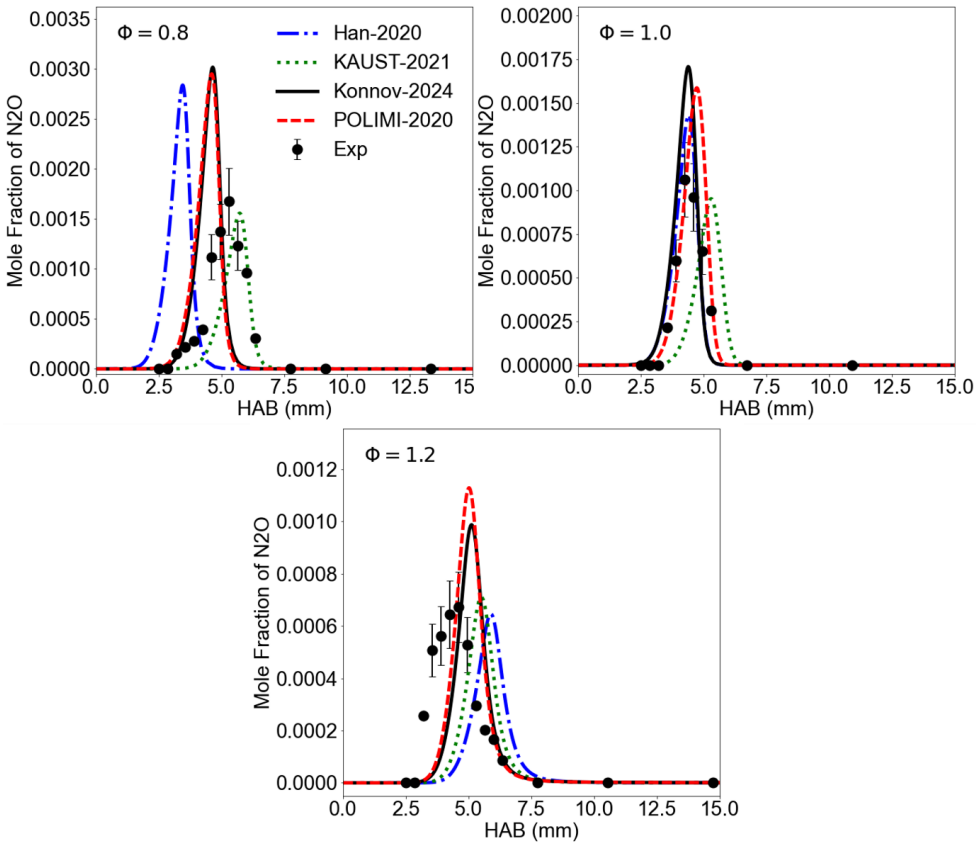

Figure 34. N_2O change with HAB. Experimental values (circles) compared with predictions of the four kinetic models (lines).

3.2.2 Hydrogen

3.2.2.1 Anisole as a tracer with Raman and LIF

Anisole ($CH_3OC_6H_5$) is a common LIF tracer for H_2, meaning that it gets seeded to provide a signal that cannot be obtained from the H_2 itself. Naturally, it is assumed that anisole follows H_2 sufficiently well in both laminar and turbulent flows. However, that was not confirmed experimentally. Thus, the goal of the present measurements was to acquire spatially resolved simultaneous signals from mixed anisole/H_2 flows and compare the overlap. The LIF signal provides information on anisole concentration, while the Raman signal captures distributions of H_2, anisole, N_2 and O_2.

Several flow conditions (Table 1) have been studied at four different heights (Figure 35) in an H_2 jet seeded with anisole.

Table 1. The experimental H_2/anisole flow conditions for the Raman/LIF measurements.

Flow rate	0.25	0.5	2	6	8
Reynolds number	31.75	63.5	253.98	2158.59	2878.52

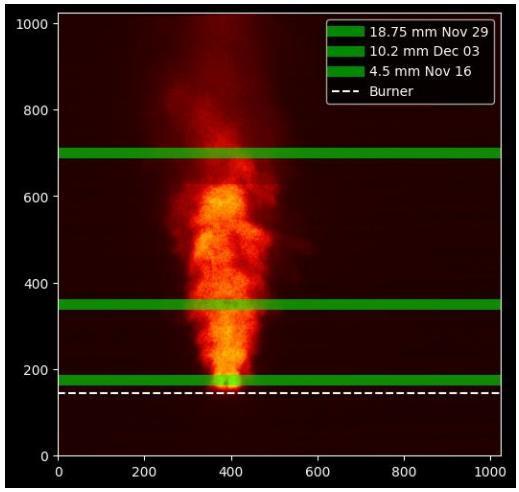

Figure 35. LIF signal of a turbulent hydrogen jet, highlighting the burner location and measurement heights for Raman spectroscopy concentration profiles.

Concentration profiles from LIF and Raman measurements were compared. Initial results suggest that in laminar or low-turbulent regions, mixing is influenced by diffusion since the LIF anisole profiles are narrower than the H_2 profiles visualized with Raman (Figure 36). However, in turbulent regions, as increased turbulence minimizes the effects of differential diffusion, the concentration profiles become consistent (Figure 37, (a)). This initial study indicated that anisole has a similar concentration distribution to H_2 under turbulent conditions.

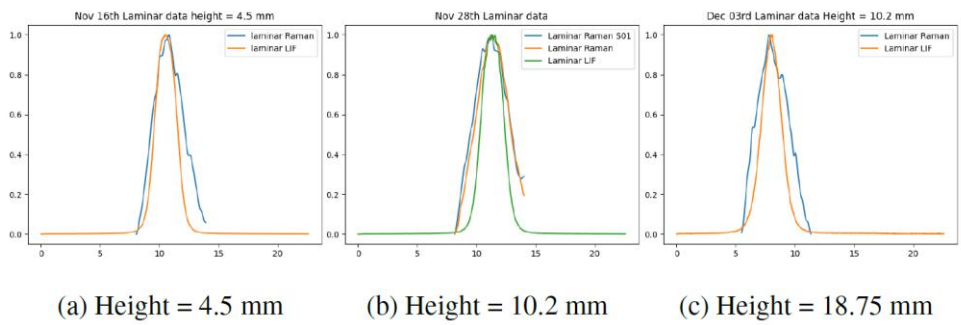

Figure 36. Comparison of concentration profiles of anisole and H_2 for laminar flows.

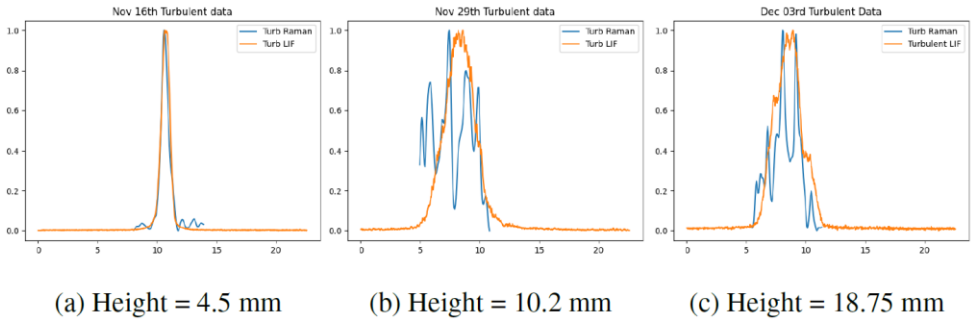

Figure 37. Comparison of concentration profiles of anisole and H_2 for turbulent flows.

Although the overall shape of the species profiles in turbulent cases is similar, the noise levels for turbulent Raman data were too high, and the comparison is difficult to perform. A way to improve the signal for Raman data has been tested by removing the spectrometer and collecting the signal directly with a camera, as described in Section 2.3.4, which resulted in at least 5 times SNR improvement and will be further studied as the final part of the work.

3.2.3 Aluminium fuels

3.2.3.1 AlO modelling and flame temperature evaluation

Metals are also of interest as carbon-free fuels, with their main advantages being high energy density, ease of storage and transportation and abundance (for example, Aluminium, discussed in the present thesis, is the third most abundant species in the earth's crust) [41]. The combustion process of metals also exhibits interesting features, such as their potential for recycling: the exhaust products substantially consist of oxides of the metal species used as the fuel, and these oxides can later be reduced back to the metals and burned once more. Another feature is the possibility of steam combustion, where the principal chemical reaction can be approximated as $Al + H_2O = AlO + H_2$, meaning that one gets H_2 as the combustion product [41]. The possibility to produce H_2 on the spot is valuable, since that fuel presents challenges regarding storage and transportation, both in terms of cost and safety [42].

For these studies, using the same PGOPHER [43] program that was previously employed for the simulation of Spontaneous Raman N_2/O_2 spectra for temperature measurements, a routine for predicting the theoretical emission spectrum of an aluminium monoxide (AlO) was developed. Similar to the N_2/O_2 Raman data, the spectral shape of an emission signal is temperature-dependent, meaning that one can obtain the experimental temperature values by matching the experimental data against the temperature-dependent simulation. The modelling was performed for the

$\Delta v = 0, \pm 1, \pm 2$ rovibrational transitions of the $X^2E^+ - B^2E^+$ band of AlO centred around 486 nm, based on the molecular data from [44-46].

The particular AlO spectra have been recorded from an Al dust flame set up as follows: a flat-flame McKenna burner was modified to have a central jet that could carry a combustion mixture different from the main flat flame [47]. The 5.33/9.13/9.29 l/min $H_2/O_2/N_2$ flat flame was used as the stabilizing pilot flame and the flow of ~60 μm sized Al particles was supplied through the middle jet mixed in the 0.4/0.2 l/min H_2/O_2 flow, which then was burned as a high-temperature flame to heat the Al particles to their ignition temperature at around 2330 K. The burnt gases from the both flames formed the oxidizing environment of hot $H_2O/O_2/N_2$ where the Al particles burned as a diffusion flame. Further details regarding the burner configuration and flame conditions can be found in literature [48, 49].

At the start, as a reference, the temperature evolution was studied based on OH chemiluminescence in a pure H_2 flame. Then, the same flame was seeded with Al particles, and once again, the OH signal was compared with the simulations. This analysis was performed with pre-existing spectral data from LIFBASE [50].

The normalized OH spectra from the two flames are presented in Figure 38, (a). As can be seen, the addition of Al altered the relative intensities of the peaks. Given that the peak intensities represent the temperature-dependent energy level population of the target molecule, relative change in intensity should be the result of a change in temperature. However, unlike the OH spectra from the pure H_2 flames, the OH spectra from the Al-seeded flames could not be fitted to the simulation predictions with satisfactory agreement. This meant that OH from the Al-seeded flames was not in thermal equilibrium. Moreover, with the addition of Al particles, the combustion medium was discovered to be optically dense enough to exhibit self-absorption. In this case, higher rotational levels (J>12) would be considered more reliable for temperature estimation [51]. However, these levels are also the ones that get excessive population due to chemical reactions which shift the system out of the thermal equilibrium, meaning that the overall temperature estimation had to be performed while trying to balance out these two opposing sources of error.

As a result, a part of the spectrum that both stayed constant with the addition of Al particles (Fig. 38, (a), highlighted in blue) and exhibited straightforward dependence on the temperature (Fig. 38, (b), highlighted in blue) was chosen as the fitting target. The resulting temperatures for the two flames were then estimated to ~2800 K (pure H_2) and ~3000 K (seeded with Al) and are presented in Table 2.

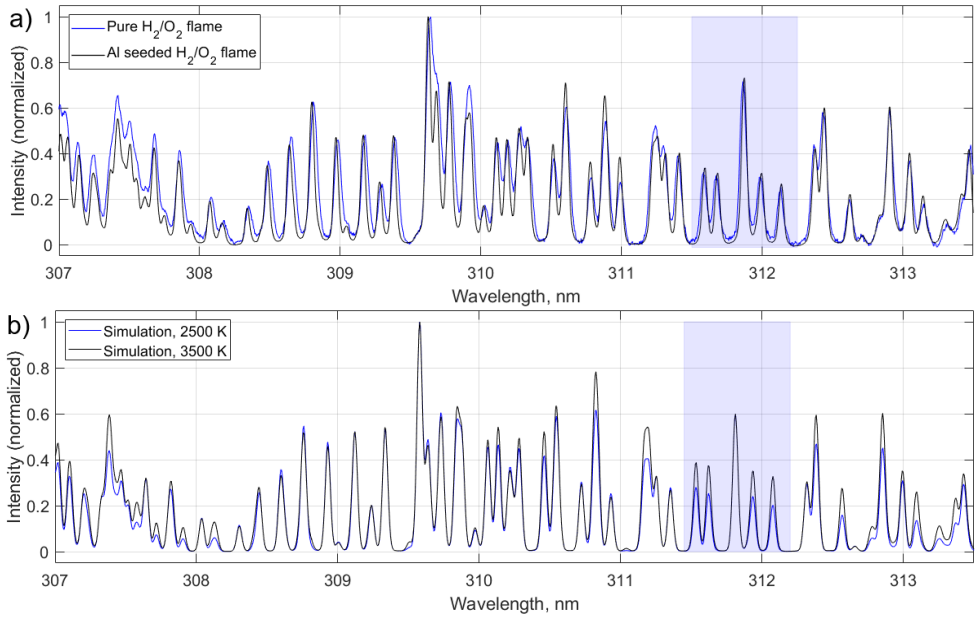

Figure 38. a) Experimental data from the two flames with the area used to extract temperature data highlighted in blue. b) OH simulation zoom-in for two different temperatures with the area used to extract temperature data highlighted in blue.

For the AlO flame data, rotational lines were first compared with the model predictions, with two bands chosen for comparison (Figure 39).

The first band chosen was $\Delta v = -1$ (Figure 39, (b)) with the choice being based on a theoretical estimation of the bands' sensitivity to temperature changes. This band exhibited the strongest relative changes in shape in the range of 500-3000 K. The second band chosen was $\Delta v = 0$ (Figure 39, (a)), due to the fact that it is a purely rotational band. This matters since vibrational transitions can take longer to reach the thermal equilibrium than rotational ones, meaning that rovibrational transitions are more likely to have their spectral shape distorted, leading to inaccurate temperature predictions.

However, as highlighted in blue in Fig. 39 (a) and (b), experimental data for the rotational spectra suffered from an interference from an unknown source that distorted the spectral shape and made the fitting routine challenging to perform. In addition, since the original spectra also required background subtraction of the black-body signal (Figure 39, black line), the resulting spectral shape appeared too distorted for higher resolution fitting, and the final temperatures could only be estimated in a relatively broad range of 3100-3500 K.

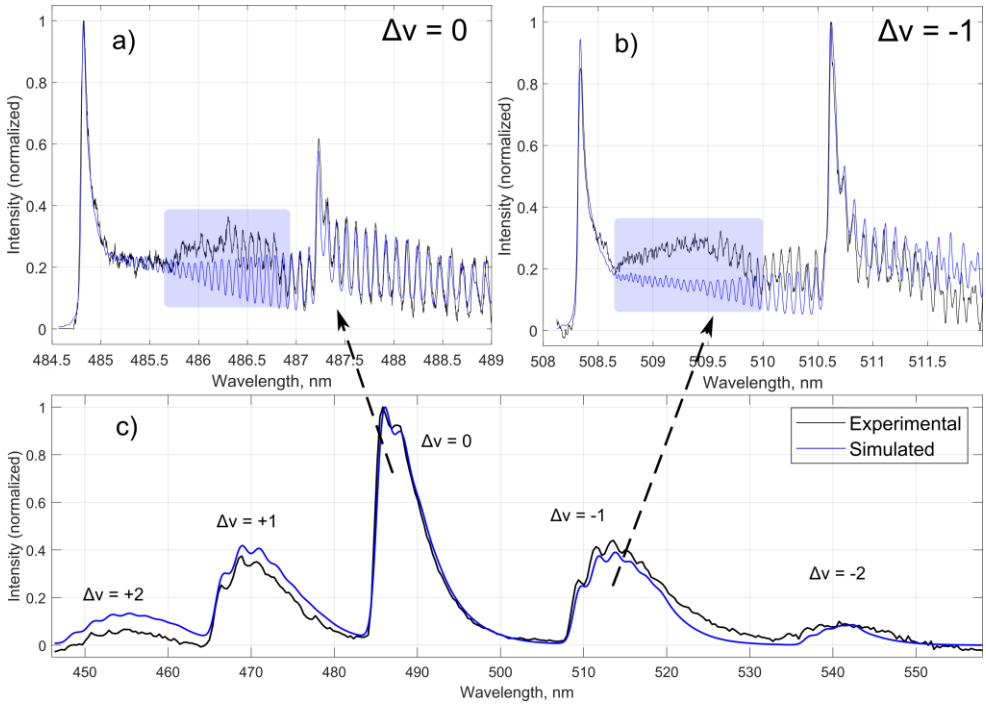

Figure 39. a-b) Simulation predictions compared with experimental data for two rotational bands of AlO. c) Simulation predictions compared with experimental data for five vibrational bands of AlO.

Lastly, two other methods were employed to obtain additional reference values for the temperature. First, vibrational spectra were fitted into the model. Comparing them to the rotational values could give an idea of the degree to which the thermal non-equilibrium can affect the temperature predictions (Figure 39, (c)). As can be seen from the graph, a satisfactory overlap between modelled and experimental spectra could not be achieved. Matching the spectra based in the left- or right-hand side bands results in around 200 K difference for the final temperature predictions with the final predictions being 3100-3300 K.

For the other method, the temperature was estimated based on the black-body radiation theory using the signal detected from the Al particles (Figure 40). There, the black line presents the wavelength-dependant experimental background which was originally subtracted through a fitting routine to obtain the AlO spectra studied above. Treating the particles as the graybody radiative heat sources means that one can estimate their temperature based on the wavelength-dependent position of the maximum, as the Wien's displacement law suggests: $\lambda_m T = 2.9 \times 10^{-3}\, m \cdot K$. However, since the AlO particles are so-called grey bodies, and not perfect black bodies, the actual energy they emit would be lower and for the proper estimation one would also have to consider their emissivity. Different sources suggest different values for it for aluminium flames, with the present study adopting two of them: the

$1/\lambda^2$ suggested by [52] and the $1/\lambda^{1.4}$ suggested by [53]. This difference resulted in around 200 K difference for the final temperature evaluation. For the reference, performing the same fit without accounting for emissivity results in up to 1000 K higher values for the estimated temperature (around 3500 K).

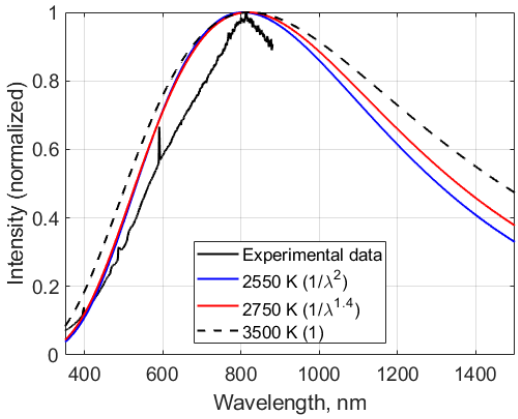

Figure 40. Temperature predictions based on black-body radiation spectral shape for three different AlO emissivity values.

The resulting temperature values from all the methods are presented in Table 2.

Table 2. Temperature predictions of the AlO flame components.

Signal source	**Temperature**
OH in a pure H2/O2 flame	2800±50 K
OH in an Al-seeded H2/O2 flame	3000±50 K
AlO rotational lines	3100-3500 K
AlO vibrational lines	3100-3300 K
Al blackbody	3500 K
Al graybody ($\varepsilon = 1/\lambda^{1.4}$)	2750 K
Al graybody ($\varepsilon = 1/\lambda^{2}$)	2550 K

Comparison with the Al particle temperature data presented by Wu et al [49] allows to draw several conclusions. First, given that the said paper reports the temperature data from the combusting particles, and present fits were performed for the surrounding gas, the expected gas temperature should be slightly lower. Given that the reported Al particle temperatures fall within 3400-3500 K, while the AlO values in this work appear to be around ~3300 K, the obtained results agree with that

expectation. However, a notable mismatch in predictions can be observed for the direct fits based on the graybody radiation, where use of blackbody emissivity value led to the most reasonable results, while the temperature fits performed using wavelength-dependent emissivity values underestimated the temperature by at least 500-300 K.

4 Conclusion

4.1 Concluding remarks

The following section contains final remarks on the experiments described in Section 3, covering them in chronological order.

Initial measurements performed with a more established DME flame allowed to, for the first time ever, quantify CH_2O as a combustion intermediate with a detection limit of around 300 ppm, as well as major species and temperature. This marked a solid start for the new measurement technique involving a multi-pass cell. However, some uncertainties regarding CH_2O cross-section data called for additional calibration measurements. These measurements have been complicated by the fact that CH_2O is highly reactive and does not exist as a stand-alone species under ambient conditions. Therefore, it was decided that the vapor phase of formalin – a $H_2O/CH_3OH/CH_2O$ mixture that is commonly used to store CH_2O – would be the measurement target. Still, as vapor-phase formalin is also reactive and the final species mole fractions cannot be estimated through routine equilibrium calculations, an additional measurement was required before that system could be used to obtain the desired CH_2O cross-section. This led to the introduction of Absorption Spectroscopy, which was used to obtain the exact species mole fractions. Finally, with the acquired cross-section data, an additional study of temperature-dependent formalin vapor composition was performed to aid with non-combustion chemistry research. This part of the work highlights how laser techniques can be used complementary to compensate for each other's weak points and illustrates that setups developed for combustion studies can also be employed for other fields, such as studies of time-evolution of reactive systems, such as formalin mixtures, at varying temperatures and pressures.

Following that, the multi-pass setup was employed to obtain minor species data from NH_3 flames that pose a bigger experimental challenge than DME. Initial measurements allowed to obtain NO data from the post-flame zone. However, strong LIF signal made it impossible to quantify anything in the reaction zone. Since the LIF signal depends on the excitation wavelength in a way that differs from Raman, the system was changed to operation at 355 nm from the initial 532 nm. This significantly reduced the LIF response and allowed the acquisition of major species data from the reaction zone. However, the conventional Raman setup is not sensitive enough for the detection of minor species. Thus, the entire multi-pass

system had to also be re-aligned for the 355 nm. Finally, this allowed to detect and quantify the reaction-zone N_2O. Both NO and N_2O mole fractions have been obtained for the first time in a pure NH_3 flame, providing invaluable data for the development of kinetic models.

The developed molecular model of aluminium monoxide (AlO) was applied to estimate the combustion temperatures of H_2/O_2 flames seeded with aluminium (Al) particles based on provided experimental data. The resulting gas-phase temperatures appeared to be in agreement with the surface particle temperatures obtained in other experiments.

Lastly, the author assisted with the research of H_2, another carbon-free fuel. This study involved a different way of using Raman spectroscopy: instead of binning the data to obtain spectral peaks, one can look at the whole camera range and use the signal to keep track of the spatial distribution of the species. In the present experiment, it was used to compare spatial distributions of N_2 and H_2 that were flowing through a burner at ambient conditions. Then, it was cross-checked with simultaneous LIF measurements of anisole to see if it follows the H_2 fuel and could be used as a tracer species to aid with H_2 studies. This, once again, illustrated that laser techniques are complementary and have a large variety of possible applications.

4.2 Future outline

Overall, the obtained data on minor species is primarily meant to assist with the development of fundamental chemical kinetic models. However, this is one of the first steps in the overall studies of a fuel: after the acquisition of the chemical data from the flat flames, increasingly complex systems are to be studied under non-ambient pressures and elevated reactant temperatures, gradually approaching the realistic operation conditions, for example, in the engines. For all these subsequent studies, the diagnostic techniques employed in this work could be of further use.

During the experiments, another gap in knowledge became apparent: not only chemical but also molecular constants data on flame radicals is extremely scarce since reaction zone measurements are challenging, and these species do not exist under ambient conditions. This significantly complicated some of the data analysis steps that would normally be handled with assistance from molecular modelling. The possibility of high-temperature measurements allows for validation of molecular models across a wider range of input conditions, and high-resolution data on temperature-induced changes to spectral shape can aid with the acquisition of molecular constants, introducing one more field the present setup could be employed in.

5 Acknowledgements

I would like to begin with a general thank you to everyone at the department for the friendly atmosphere and weekly fika, even if I was not always present.

Thank you to my supervisor, Christian Brackmann, and my co-supervisor, Anna-Lena Såhlberg, for all the hands-on help with the lab work and general guidance with the studies.

Thank you to my former colleague, Haisol Kim, for all the help starting out, helping me to find a place to stay in Lund and contributing to me getting a cat to take care of. Thank you to the group that started with me, Jundie Chen, Yue Qiu, and Zhiyong Wu, for keeping me company. Thank you to Megha Prakash for helping me take care of the lab. Thank you to Aravind Sridhara for putting additional effort so that our research could be included in my thesis.

Thank you to David Sanned, Meng Li, Meena Raveesh and Lisa Rämisch, even if we started at different times and never worked together directly, I treasured your company. Thank you to Yupan Bao and Ruike Bi for the assistance with Copenhagen travels last year and thank you to Jinguo Sun for the assistance with Python.

Thank you to the seniors at the department for being available for various questions.

Thank you to my friends I have not seen in a while, for still keeping me company from far away.

Thank you to my parents, Ayrat and Larisa, for always supporting me.

Lastly, I would like to thank the COCALD project for the provided funding.

6 References

[1] J. Warnatz, U. Maas, R.W. Dibble, Combustion : physical and chemical fundamentals, modeling and simulation, experiments, pollutant formation, 4th ed., Springer, Berlin ; New York, 2006.

[2] G. Vourliotakis, G. Skevis, M.A. Founti, Some aspects of combustion chemistry of C1-C2 oxygenated fuels in low pressure premixed flames, P Combust Inst 35 (2015) 437-445.

[3] Y.G. Ju, C.B. Reuter, O.R. Yehia, T.I. Farouk, S.H. Won, Dynamics of cool flames, Prog Energ Combust 75 (2019).

[4] W. Demtröder, Laser spectroscopy : basic concepts and instrumentation, 3rd ed., Springer, Berlin ; New York, 2003.

[5] D.A. Long, Raman spectroscopy, McGraw-Hill, New York, 1977.

[6] G. Herzberg, Molecular spectra and molecular structure, 2nd ed., R.E. Krieger Pub. Co., Malabar, Fla., 1989.

[7] J. Hawkes, I. Latimer, Lasers : theory and practice, Prentice Hall, New York, 1995.

[8] S. Nilsson, E. Kristensson, M. Aldén, J. Bood, A. Ehn, Fluorescence lifetime imaging through scattering media, Sci Rep-Uk 13 (2023).

[9] A. Ehn, O. Johansson, A. Arvidsson, M. Aldén, J. Bood, Single-laser shot fluorescence lifetime imaging on the nanosecond timescale using a Dual Image and Modeling Evaluation algorithm, Opt Express 20 (2012) 3043-3056.

[10] M. Raveesh, A. Dominguez, M. Linne, J. Bood, A. Hosseinnia, Interferometric quantum control (IQC) by fs/ns rotational coherent anti-Stokes Raman spectroscopy (RCARS), Opt Express 31 (2023) 38064-38076.

[11] A.L. Sahlberg, J. Zhou, M. Aldén, Z.S. Li, Non-intrusive detection of methyl chloride in hot gas flows using infrared degenerate four-wave mixing, J Raman Spectrosc 46 (2015) 695-701.

[12] Z.W. Sun, Development and application of non-linear mid-infrared laser spectroscopy for combustion diagnostics, Department of Physics, Division of Combustion Physics, Lund University, Lund, Sweden, 2012.

[13] J. Kiefer, P. Ewart, Laser diagnostics and minor species detection in combustion using resonant four-wave mixing, Prog Energ Combust 37 (2011) 525-564.

[14] A.H. Zewail, Society of Photo-optical Instrumentation Engineers., IEEE Computer Society., Advances in laser spectroscopy I, August 23-24, 1977, San Diego, California, SPIE, Bellingham, Wash., 1977.

[15] J. Walewski, C.F. Kaminski, S.F. Hanna, R.P. Lucht, Dependence of partially saturated polarization spectroscopy signals on pump intensity and collision rate, Phys Rev A 64 (2001).

[16] T.A. Reichardt, R.P. Lucht, Theoretical calculation of line shapes and saturation effects in polarization spectroscopy, J Chem Phys 109 (1998) 5830-5843.

[17] T.A. Reichardt, W.C. Giancola, R.P. Lucht, Experimental investigation of saturated polarization spectroscopy for quantitative concentration measurements, Appl Optics 39 (2000) 2002-2008.

[18] K.C. Utsav, P.L. Varghese, Accurate temperature measurements in flames with high spatial resolution using Stokes Raman scattering from nitrogen in a multiple-pass cell, Appl Optics 52 (2013) 5007-5021.

[19] H. Kim, A. Zubairova, M. Alden, C. Brackmann, Signal-enhanced Raman spectroscopy with a multi-pass cavity for quantitative measurements of formaldehyde, major species and temperature in a one-dimensional laminar DME-air flame, Combust Flame 244 (2022).

[20] S.M. Burke, W. Metcalfe, O. Herbinet, F. Battin-Leclerc, F.M. Haas, J. Santner, F.L. Dryer, H.J. Curran, An experimental and modeling study of propene oxidation. Part 1: Speciation measurements in jet-stirred and flow reactors, Combust Flame 161 (2014) 2765-2784.

[21] S.M. Burke, U. Burke, R. Mc Donagh, O. Mathieu, I. Osorio, C. Keesee, A. Morones, E.L. Petersen, W.J. Wang, T.A. DeVerter, M.A. Oehlschlaeger, B. Rhodes, R.K. Hanson, D.F. Davidson, B.W. Weber, C.J. Sung, J. Santner, Y.G. Ju, F.M. Haas, F.L. Dryer, E.N. Volkov, E.J.K. Nilsson, A.A. Konnov, M. Alrefae, F. Khaled, A. Farooq, P. Dirrenberger, P.A. Glaude, F. Battin-Leclerc, H.J. Curran, An experimental and modeling study of propene oxidation. Part 2: Ignition delay time and flame speed measurements, Combust Flame 162 (2015) 296-314.

[22] C.W. Zhou, Y. Li, E. O'Connor, K.P. Somers, S. Thion, C. Keesee, O. Mathieu, E.L. Petersen, T.A. DeVerter, M.A. Oehlschlaeger, G. Kukkadapu, C.J. Sung, M. Alrefae, F. Khaled, A. Farooq, P. Dirrenberger, P.A. Glaude, F. Battin-Leclerc, J. Santner, Y.G. Ju, T. Held, F.M. Haas, F.L. Dryer, H.J. Curran, A comprehensive experimental and modeling study of isobutene oxidation, Combust Flame 167 (2016) 353-379.

[23] J. Brandmuller, Rayleigh-Streuung Und Rotations-Raman-Effekt Von Flussigkeiten, Z Phys 140 (1955) 75-91.

[24] W.F. Murphy, W. Holzer, H.J. Bernstein, Gas Phase Raman Intensities - a Review of Pre-Laser Data, Appl Spectrosc 23 (1969) 211-+.

[25] S.F. Rice, T.B. Hunter, A.C. Ryden, R.G. Hanush, Raman spectroscopic measurement of oxidation in supercritical water .1. Conversion of methanol to formaldehyde, Ind Eng Chem Res 35 (1996) 2161-2171.

[26] M. Albert, B.C. García, C. Kuhnert, R. Peschla, G. Maurer, Vapor-liquid equilibrium of aqueous solutions of formaldehyde and methanol, Aiche J 46 (2000) 1676-1687.

[27] I.E. Gordon, L.S. Rothman, R.J. Hargreaves, R. Hashemi, E.V. Karlovets, F.M. Skinner, E.K. Conway, C. Hill, R.V. Kochanov, Y. Tan, P. Wcislo, A.A. Finenko, K. Nelson, P.F. Bernath, M. Birk, V. Boudon, A. Campargue, K.V. Chance, A. Coustenis, B.J. Drouin, J.M. Flaud, R.R. Gamache, J.T. Hodges, D. Jacquemart, E.J. Mlawer, A.V. Nikitin, V.I. Perevalov, M. Rotger, J. Tennyson, G.C. Toon, H. Tran, V.G. Tyuterev, E.M. Adkins, A. Baker, A. Barbe, E. Canè, A.G. Császár, A. Dudaryonok, O. Egorov, A.J. Fleisher, H. Fleurbaey, A. Foltynowicz, T. Furtenbacher, J.J. Harrison, J.M. Hartmann, V.M. Horneman, X. Huang, T. Karman, J. Karns, S. Kassi, I. Kleiner, V. Kofman, F. Kwabia-Tchana, N.N. Lavrentieva, T.J. Lee, D.A. Long, A.A. Lukashevskaya, O.M. Lyulin, V.Y. Makhnev, W. Matt, S.T. Massie, M. Melosso, S.N. Mikhailenko, D. Mondelain, H.S.P. Müller, O.V. Naumenko, A. Perrin, O.L. Polyansky, E. Raddaoui, P.L. Raston, Z.D. Reed, M. Rey, C. Richard, R. Tóbiás, I. Sadiek, D.W. Schwenke, E. Starikova, K. Sung, F. Tamassia, S.A. Tashkun, J. Vander Auwera, I.A. Vasilenko, A.A. Vigasin, G.L. Villanueva, B. Vispoel, G. Wagner, A. Yachmenev, S.N. Yurchenko, The HITRAN2020 molecular spectroscopic database, J Quant Spectrosc Ra 277 (2022).

[28] P. Glarborg, J.A. Miller, B. Ruscic, S.J. Klippenstein, Modeling nitrogen chemistry in combustion, Prog Energ Combust 67 (2018) 31-68.

[29] E.C. Okafor, Y. Naito, S. Colson, A. Ichikawa, T. Kudo, A. Hayakawa, H. Kobayashi, Experimental and numerical study of the laminar burning velocity of CH_4-NH_3-air premixed flames, Combust Flame 187 (2018) 185-198.

[30] A. Stagni, C. Cavallotti, S. Arunthanayothin, Y. Song, O. Herbinet, F. Battin-Leclerc, T. Faravelli, An experimental, theoretical and kinetic-modeling study of the gas-phase oxidation of ammonia, React Chem Eng 5 (2020) 696-711.

[31] X.L. Han, M.L. Lavadera, A.A. Konnov, An experimental and kinetic modeling study on the laminar burning velocity of NH3+N2O+air flames, Combust Flame 228 (2021) 13-28.

[32] J. Lill, M. Stark, R. Schultheis, A. Weinmann, A. Dreizler, D. Geyer, Towards non-intrusive, quantitative N_2O Raman measurements in ammonia flames, P Combust Inst 40 (2024).

[33] C. Brackmann, T. Methling, M.L. Lavadera, G. Capriolo, A.A. Konnov, Experimental and modeling study of nitric oxide formation in premixed methanol plus air flames, Combust Flame 213 (2020) 322-330.

[34] Z.W. Sun, Z.S. Li, A.A. Konnov, M. Aldén, Quantitative HCN measurements in $CH_4/N_2O/O_2/N_2$ flames using mid-infrared polarization spectroscopy, Combust Flame 158 (2011) 1898-1904.

[35] Z.W. Sun, Z.S. Li, B. Li, Z.T. Alwahabi, M. Aldén, Quantitative C_2H_2 measurements in sooty flames using mid-infrared polarization spectroscopy, Appl Phys B-Lasers O 101 (2010) 423-432.

[36] P. Glarborg, C.S. Andreasen, H. Hashemi, R.C. Qian, P. Marshall, Oxidation of methylamine, Int J Chem Kinet 52 (2020) 893-906.

[37] A.A. Konnov, J. Chen, M.L. Lavadera, Measurements of the laminar burning velocities of 1,2-butadiene: A comparative study, P Combust Inst 40 (2024).

[38] X.Y. Zhang, S.P. Moosakutty, R.P. Rajan, M. Younes, S.M. Sarathy, Combustion chemistry of ammonia/hydrogen mixtures: Jet-stirred reactor measurements and comprehensive kinetic modeling, Combust Flame 234 (2021).

[39] X.L. Han, Z.H. Wang, Y. He, Y.Q. Zhu, K.F. Cen, Experimental and kinetic modeling study of laminar burning velocities of NH3/syngas/air premixed flames, Combust Flame 213 (2020) 1-13.

[40] J.D. Chen, X.L. Han, A.A. Konnov, Data consistency of the laminar burning velocity of oxygen-enriched NH3+O2+N2 mixtures and kinetic modeling, Fuel 385 (2025).

[41] J.M. Bergthorson, Recyclable metal fuels for clean and compact zero-carbon power, Prog Energ Combust 68 (2018) 169-196.

[42] M.L. Yue, H. Lambert, E. Pahon, R. Roche, S. Jemei, D. Hissel, Hydrogen energy systems: A critical review of technologies, applications, trends and challenges, Renew Sust Energ Rev 146 (2021).

[43] C.M. Western, PGOPHER: A program for simulating rotational, vibrational and electronic spectra, J Quant Spectrosc Ra 186 (2017) 221-242.

[44] O. Launila, L.E. Berg, Spectroscopy of AlO: Combined analysis of the $A^2\Pi i \rightarrow X^2\Sigma+$ and $B^2\Sigma^+ \rightarrow X^2\Sigma^+$ transitions, J Mol Spectrosc 265 (2011) 10-14.

[45] C.G. Parigger, J.O. Hornkohl, Computation of AlO $B^2\Sigma^+ \rightarrow X^2\Sigma^+$ emission spectra, Spectrochim Acta A 81 (2011) 404-411.

[46] J.A. Coxon, S. Naxakis, Rotational Analysis of the $B^2\Sigma^+ \rightarrow X^2\Sigma^+$ System of the Aluminum Monoxide Radical, AlO, J Mol Spectrosc 111 (1985) 102-113.

[47] Flat Flame Burner, Holthuis and Associates. http://www.flatflame.com.

[48] Z.Y. Wu, C. Ruan, Y. Qiu, M. Stiti, S.J. Xu, N. Jüngst, E. Berrocal, M. Aldén, X.S. Bai, Z.S. Li, Flame structure of single aluminum droplets burning in hot steam-dominated flows, Combust Flame 271 (2025).

[49] Z.Y. Wu, C. Ruan, M. Stiti, S.J. Xu, X.S. Bai, E. Berrocal, M. Ald, Z.S. Li, Spatiotemporally resolved surface temperature measurement of aluminum ignition and combustion in steam and oxygenated environments, Combust Flame 264 (2024).

[50] J. Luque, Crosley, D.R., LIFBASE: Database and Spectral Simulation Program (Version 1.5), SRI International Report MP 99 (1999).

[51] A. Brockhinke, J. Krüger, M. Heusing, M. Letzgus, Measurement and simulation of rotationally-resolved chemiluminescence spectra in flames, Appl Phys B-Lasers O 107 (2012) 539-549.

[52] S. Goroshin, J. Mamen, A. Higgins, T. Bazyn, N. Glumac, H. Krier, Emission spectroscopy of flame fronts in aluminum suspensions, P Combust Inst 31 (2007) 2011-2019.

[53] J. Kalman, D. Allen, N. Glumac, H. Krier, Optical Depth Effects on Aluminum Oxide Spectral Emissivity, J Thermophys Heat Tr 29 (2015) 74-82.

Printed by Media-Tryck, Lund 2025 NORDIC SWAN ECOLABEL 3041 0903

Faculty of Engineering
Department of Physics
Division of Combustion Physics

LRCP-269
ISBN 978-91-8104-557-4
ISSN 1102-8718